

# Expanding Universal Machine Learning Interatomic Potentials to 97 Elements Towards Nuclear Applications

Naoya Kuroda,<sup>1,\*</sup> Kenji Ishihara,<sup>1,2,\*</sup> Tomoya Shiota,<sup>1,†</sup> and Wataru Mizukami<sup>1,‡</sup>

<sup>1</sup>*Center for Quantum Information and Quantum Biology,  
The University of Osaka, 1-2 Machikaneyama, Toyonaka 560-8531, Japan*

<sup>2</sup>*Graduate School of Science, The University of Osaka,  
1-1 Machikaneyama, Toyonaka, Osaka 560-0043, Japan*

(Dated: March 4, 2026)

Machine learning interatomic potentials (MLIPs) evaluate potential energy surfaces orders of magnitude faster while maintaining accuracy comparable to first-principles calculations, and universal MLIPs that cover most of the periodic table are becoming increasingly commonplace. However, existing large-scale datasets have limited or no coverage of heavy elements such as minor actinides crucial in the nuclear field, and universal MLIPs are typically limited to 89 elements. Here, we constructed a heavy element dataset HE26 containing minor actinides, based on experimental and computational literature data. By integrating this with existing molecular and crystal datasets, we developed an open-source universal MLIP covering 97 elements, the broadest elemental coverage to date. The resulting model showed strong performance on the inorganic MPtrj and organic OFF23 test sets and promising accuracy on HE26. The dataset and model open a pathway toward the development of energy resources and the design of novel materials, such as actinide-based high-entropy ceramics, in the nuclear field.

## I. INTRODUCTION

Minor actinide elements, including transuranium elements such as Am, Cm, and Cf, are not merely nuclear waste but key resources for the sustainability of the nuclear fuel cycle [1–5], and are emerging as crucial components in advanced applications ranging from americium oxide for space exploration radioisotope thermoelectric generators [6–8] to actinide-bearing high-entropy ceramics designed for extreme environments [9–11]. Unfortunately, due to their strong radioactivity and toxicity, experimental measurements of important thermophysical properties, such as lattice thermal conductivity, linear thermal expansion, and viscosity, are extremely difficult and expensive, leaving the thermophysical and thermochemical properties of many minor actinide compounds largely unexplored [12–23]. Theoretical and computational approaches are therefore essential for characterizing these materials.

Computational prediction of thermophysical properties relies on the accuracy of the underlying interatomic potential. First-principles calculations based on density functional theory (DFT) can model interatomic forces accurately, but their computational cost becomes prohibitive for multi-component systems: the reduced crystal symmetry requires large supercells, and the number of atomic displacement configurations needed for higher-order anharmonic force constants grows rapidly [24]. Machine learning interatomic potentials (MLIPs) offer a practical route to overcome this bottleneck [25–30]. MLIPs evaluate potential-energy surfaces orders of

magnitude faster than DFT while maintaining near-DFT accuracy.

System-specific MLIPs, trained on first-principles data for particular systems, have recently predicted the high-temperature thermophysical properties of nuclear materials such as  $\text{UO}_2$  and  $\text{ThO}_2$  with accuracy approaching that of DFT [31–36]. However, because these models are trained on individual systems, they are not suitable for screening across broad compositional spaces, such as actinide-containing mixed oxide fuels [1–5].

Universal MLIPs, also known as atomistic foundation models, are emerging to address this limitation as transferable interatomic potentials that cover a wide range of elements [28]. Architectural developments, such as graph neural networks (GNNs) [37] and  $E(3)$ -equivariant message passing [38–40], together with advances in distributed scalability [41] and more efficient equivariant architectures [42], have driven recent progress. Pretraining with large-scale open datasets [43–47] and heterogeneous training datasets [48–54] has further improved these models, enabling application to molecules, crystals, and surface systems. However, existing universal MLIPs typically do not cover transuranium elements such as Am, Cm, and Cf [48–55]. This gap comes from the limited or absent coverage of heavy elements in current first-principles datasets [43, 56], which restricts the applicability of pretrained universal models not only to actinide mixed oxides but even to many heavy-element compounds.

To expand the elemental coverage of a universal MLIP, we develop a DFT dataset, Heavy Element 2026 (HE26). HE26 spans 65 elements in total and contains eight heavy elements (Am, Cm, Cf, Fr, At, Ra, Po, and Rn) that are rarely present in existing large-scale datasets. The HE26 dataset consists of three subsets: (1) Basic Heavy Element (BHE): elemental solids and binary ox-

\* These two authors contributed equally to this work.

† shiota.tomoya.ss@gmail.com

‡ mizukami.wataru.qiqb@osaka-u.ac.jp

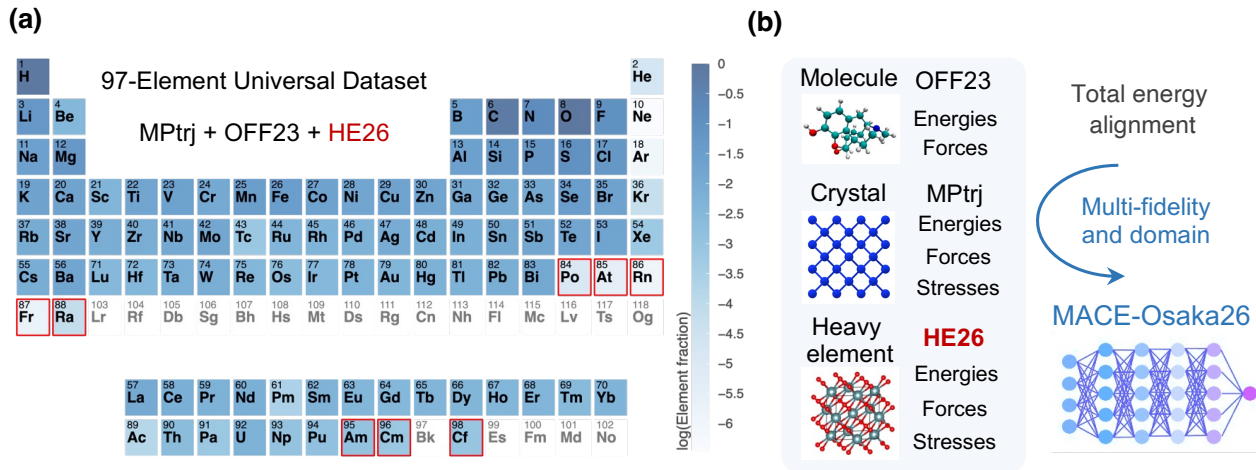


FIG. 1. Overview of the 97-element universal dataset and the MACE-Osaka26 model. (a) Periodic table showing the element distribution (log scale) of the combined dataset consisting of MPtrj, OFF23, and our HE26 dataset. Red boxes indicate the heavy elements newly added in this study. (b) Schematic of the training pipeline integrating molecular (OFF23) and crystal (MPtrj, HE26) data via the total energy alignment protocol.

ides; (2) Complex Heavy Element (CHE): diverse multicomponent systems; and (3) Compositionally Complex Fluorite Oxides (CCFO): binary-to-quinary fluorite-type mixed oxides of actinides, lanthanides, and rare earth elements, targeting actinide-based high-entropy ceramics and minor-actinide mixed-oxide fuels. We integrate HE26 with the OFF23 [57] and MPtrj [55] datasets unified via the total-energy alignment (TEA) protocol [48]. Using this combined dataset, we train MACE-Osaka26, an open-source universal MLIP covering 97 elements. We demonstrate the model’s applicability by predicting lattice parameters and thermal conductivity of actinide fluorite oxides, including mixed oxides containing minor actinides.

The remainder of this paper is organized as follows. Section II presents results in three parts: cross-domain accuracy of MACE-Osaka26 across crystalline, molecular, and heavy element datasets; detailed evaluation on the HE26 dataset; and lattice thermal conductivity predictions for actinide fluorite oxides. Section III discusses the origins of the model’s performance and remaining limitations. Section IV summarizes our findings and outlook. Section V describes the dataset construction, MLIP training, and thermal conductivity calculation procedures.

## II. RESULTS

We first evaluate the cross-domain generalization capability of the MACE-Osaka26 model across molecules, crystals, and heavy-element compounds spanning 97 elements. Table I and Figure 2 compare the prediction accuracies of MACE-Osaka24 and MACE-Osaka26 across

crystalline (MPtrj), molecular (OFF23), and heavy-element (HE26) datasets. Appendix B provides detailed descriptions of the prediction accuracies for energies on the test sets, and for forces and stresses on both the training and test sets. As shown in Table I, the prediction accuracies for the training and test sets exhibit generally similar trends across the MPtrj and OFF23 datasets. Furthermore, due to the limited total number of structures in the HE26 dataset, a separate test set was not partitioned. For these reasons, the parity plots illustrating the energy prediction accuracies in Figure 2 are presented using the training sets for all three datasets.

For the crystalline MPtrj dataset, MACE-Osaka26 shows consistent improvements in energy prediction on the test set, with the mean absolute error (MAE) decreasing from 33.7 to 29.3 meV/atom and the root-mean-square error (RMSE) from 77.2 to 62.0 meV/atom. While the force MAE slightly increased, the force RMSE and stress RMSE showed meaningful reductions, indicating better handling of outlier configurations in bulk systems. The most striking improvement is observed in the molecular OFF23 test set. MACE-Osaka26 significantly enhanced energy accuracy compared to MACE-Osaka24, notably halving the RMSE from 25.2 to 12.3 meV/atom. This significant improvement in molecular OFF23 suggests that MACE-Osaka26 has robust generalization capabilities not only for periodic bulk crystals but also for isolated molecular systems.

### A. Cross-domain Accuracy

Furthermore, the results on the HE26 dataset underscore the model’s expanded chemical coverage. While

TABLE I. Performance comparison between MACE-Osaka24 and MACE-Osaka26. Accuracies for energy, force, and stress are evaluated. For MPtrj and OFF23, metrics are reported on both the training and test sets; for the HE26 dataset, metrics are on the training and validation sets. Benchmark accuracies are evaluated using two metrics: mean absolute error (MAE) and root mean square error (RMSE). The values outside and inside the parentheses represent the MAE and RMSE, respectively.

Dataset	Split	# Structures	Model	Energy MAE (RMSE) (meV/atom)	Force MAE (RMSE) (meV/Å)	Stress MAE (RMSE) (meV/Å <sup>3</sup> )
MPtrj (Crystalline)	Train	1,502,422	MACE-Osaka24	31.4 (74.6)	47.4 ( <b>117.0</b> )	<b>1.7 (10.3)</b>
			MACE-Osaka26	<b>26.8 (60.5)</b>	<b>47.3 (148.3)</b>	1.7 (10.4)
	Test	77,973	MACE-Osaka24	33.7 (77.2)	<b>61.9 (144.3)</b>	2.2 (45.8)
			MACE-Osaka26	<b>29.3 (62.0)</b>	62.4 ( <b>140.7</b> )	<b>2.2 (35.8)</b>
OFF23 (Molecular)	Train	951,005	MACE-Osaka24	5.7 (26.6)	<b>39.9 (78.1)</b>	N/A
			MACE-Osaka26	<b>4.9 (11.9)</b>	44.5 (88.0)	N/A
	Test	50,195	MACE-Osaka24	5.8 (25.2)	<b>41.2 (130.7)</b>	N/A
			MACE-Osaka26	<b>5.0 (12.3)</b>	45.7 (137.1)	N/A
HE26 (Actinides etc.)	Train	59,438	MACE-Osaka24	N/A <sup>a</sup>	N/A <sup>a</sup>	N/A <sup>a</sup>
			MACE-Osaka26	<b>44.7 (117.3)</b>	<b>26.3 (73.7)</b>	<b>1.3 (7.4)</b>

<sup>a</sup> MACE-Osaka24 does not support the heavy elements included in HE26 dataset.

MACE-Osaka24 did not support the eight heavy elements (e.g., Am, Cm, and Cf) included in this dataset, MACE-Osaka26 successfully incorporates them, achieving an energy MAE of 44.7 meV/atom and an RMSE of 117.3 meV/atom on the training set (Figure 2(c)). Notably, the force and stress accuracies for this dataset are remarkably high (force MAE: 26.3 meV/Å; stress MAE: 1.3 meV/Å<sup>3</sup>), confirming that the model effectively learns the complex potential energy surfaces of heavy-element compounds despite the limited dataset size. These results demonstrate that MACE-Osaka26 is a universal potential, capable of providing reliable predictions across a diverse chemical space of 97-elements.

## B. Detailed Evaluation on HE26 Dataset

Having established the broad cross-domain accuracy of MACE-Osaka26 spanning 97 elements, we now conduct a detailed evaluation focusing specifically on the HE26 dataset. Developing robust MLIPs for heavy elements—particularly actinides and lanthanides—presents a formidable challenge due to their intricate electronic structures and the inherent scarcity of reliable DFT training data. To systematically assess the model’s predictive capabilities, physical fidelity, and generalization robustness, we analyze its performance across three subsets of increasing compositional and structural complexity: (1) elemental solids and binary oxides (BHE), (2) diverse multi-component systems (CHE), and (3) binary-to-quinary compositionally complex fluorite oxides (CCFO).

### 1. Elemental Solids and Binary Oxides

We evaluated the prediction accuracy of lattice parameters (defined as the average length of the unit cell lattice vectors) for the BHE subset of HE26 dataset, which consists of 42 unique structures. Figure 3(a) presents the

parity plot comparing the lattice parameters predicted by MACE-Osaka26 against the DFT reference values. The model achieves an overall RMSE of 0.4488 Å. The model demonstrates high accuracy for actinide elements such as Am and Cm, yielding near-zero errors for both elemental solids and oxides. Conversely, noticeable deviations are observed for specific structures containing Ra, At, and Cf. These deviations are largely attributed to the extreme difficulty in achieving electronic convergence in DFT calculations for these specific heavy elements, which inherently limits the amount of available training data. Nevertheless, the parity plot indicates that MACE-Osaka26 correctly captures the overall structural scale across diverse systems, confirming its viability as a solid baseline model even in regions with sparse reference data.

### 2. Multi-Component Systems

Building upon the baseline performance, we further assessed the model on the CHE subset of HE26 dataset. This dataset encompasses 136 unique structures and covers a remarkably broad chemical space comprising 64 different element types (excluding At). As shown in Figure 3(b), the MLIP predictions for the CHE subset are in good agreement with the DFT reference, achieving a very low RMSE of 0.0477 Å. This is an order of magnitude smaller than the 0.4488 Å RMSE for the BHE subset shown in Figure 3(a). Three structures were excluded from the analysis because their geometry optimization failed to converge. Remarkably, the model maintains this high accuracy across diverse chemical environments, including experimentally synthesized representative structures such as the Am(III) N,N-di-2-ethylhexyl-6-amide-pyridine-2-carboxylic acid (DE-HAPA) complex [58] and Cf oxyfluoride Cf<sub>8</sub>O<sub>8</sub>F<sub>8</sub> [59] (illustrated as insets in Figure 3(b)). The comprehensive elemental coverage and composition of this subset are given in the Appendix (Tables IV and V). The consis-

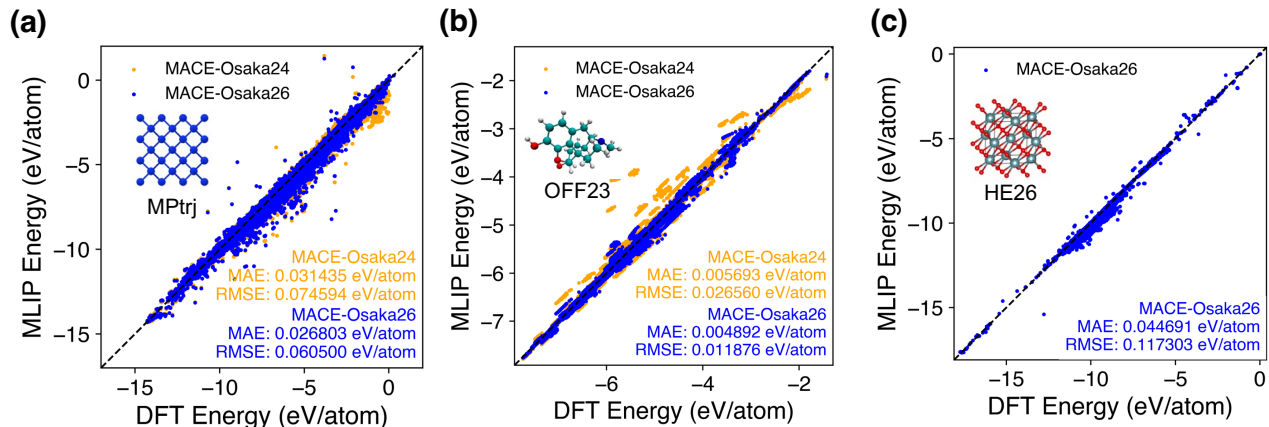


FIG. 2. Accuracy comparison between MACE-Osaka24 and MACE-Osaka26 on cross-domain systems. (a) Evaluation on the MPtrj training set representing crystalline systems, and (b) the OFF23 training set representing molecular systems, using both MACE-Osaka24 (orange) and MACE-Osaka26 (blue) models. (c) Results for the HE26 training set containing heavy elements. Note that only MACE-Osaka26 is shown in (c) as it incorporates eight heavy elements not supported by the MACE-Osaka24 model. Mean absolute errors (MAE) and root-mean-square errors (RMSE) are provided in eV/atom. Here, the main difference in the architecture between MACE-Osaka24 and MACE-Osaka26 is that their graph cutoff values are 4.5 Å and 6.0 Å, respectively.

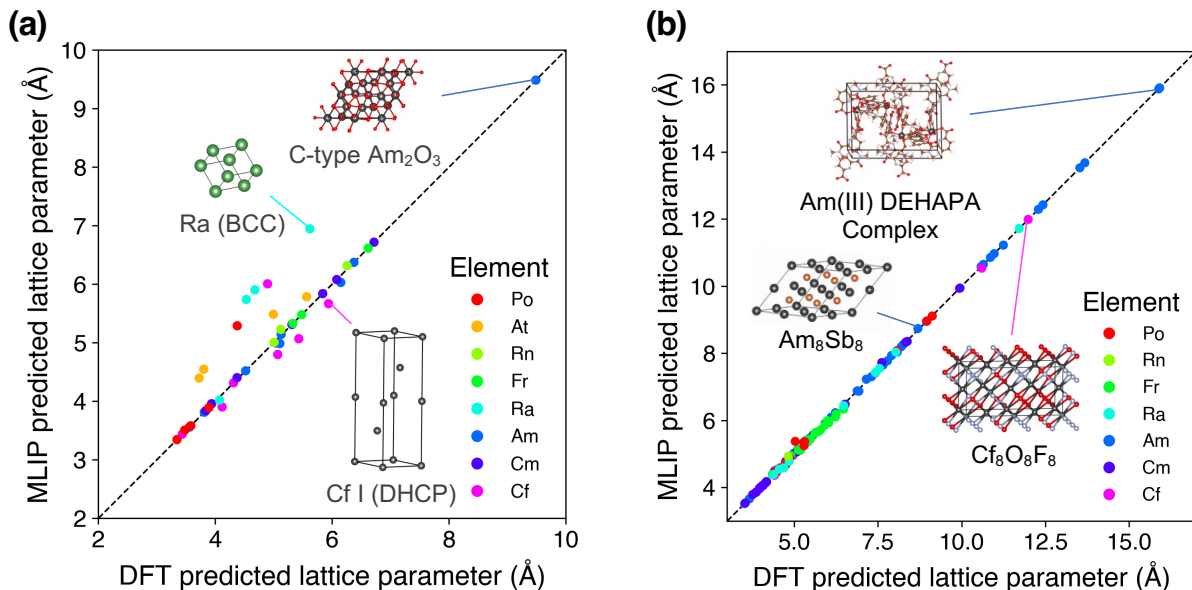


FIG. 3. Parity plots of DFT-calculated versus MLIP-predicted lattice parameters for heavy element systems. (a) The Basic Heavy Element (BHE) subset, comprising 42 unique structures. (b) The Complex Heavy Element (CHE) subset, comprising 133 unique structures. Three structures were excluded because their structural optimizations did not converge. The specific systems illustrated in the insets represent typical experimentally synthesized examples. The lattice parameter of each structure is defined throughout this paper as the average length of the unit cell lattice vectors.

tently minimal errors across these 133 diverse structures demonstrate that MACE-Osaka26 successfully generalizes to multi-component heavy-element systems without experiencing performance degradation.

### 3. Compositionally Complex Fluorite Oxides

Finally, we evaluated the model’s performance on the CCFO subset, which encompasses solid solutions ranging from binary to quinary systems. A significant challenge for MLIPs is not merely minimizing the mathematical error against DFT, but accurately capturing the underlying physical and chemical trends across the periodic table.

As shown in Figure 4(a), MACE-Osaka26 reproduces the DFT reference values across the actinide series (Th to Cf) with an RMSE of 0.0067 Å. However, a noticeable discrepancy between the computational results and the experimental data appears around Am and Cm. While experiments show a monotonic decrease in the lattice constant associated with actinide contraction, the DFT data predict a slight increase at Cm. This deviation suggests that, although the MLIP properly learns the provided potential-energy surface, the PBE-based DFT approach adopted in this study may not fully describe the complex behavior of strongly correlated  $f$  electrons in the heavier actinides. Nevertheless, the model’s ability to closely follow the DFT trend supports its reliability as an emulator. Similarly, for fluorite-structured oxides containing various transition metals and lanthanides (Figure 4(b)), the model captures the structural variations with a low RMSE of 0.0124 Å.

To further assess the model’s robustness against compositional complexity, we analyzed the prediction accuracy as a function of the number of constituent elements (excluding oxygen). The parity plot in Figure 4(c) illustrates a tight correlation between the MLIP predictions and DFT calculations, irrespective of the system’s complexity. The detailed error distributions are shown in Figure 4(d, e), and the quantitative metrics are summarized in Table II. Although the RMSE slightly increases from 0.0103 Å for binary systems to 0.0170 Å for quinary systems, the mean absolute error (MAE) remains exceptionally low ( $\sim 0.005$  Å) and highly consistent across all complexity levels. These findings confirm that

TABLE II. Error statistics of the MACE-Osaka26 model for predicting lattice parameters of compositionally complex fluorite oxides, categorized by the number of constituent elements (excluding oxygen). MaxAE denotes the maximum absolute error.

# Elements	# Structures	RMSE (Å)	MAE (Å)	MaxAE (Å)
1	17	0.0103	0.0071	0.0335
2	324	0.0142	0.0050	0.2090
3	1691	0.0158	0.0049	0.2223
4	1946	0.0170	0.0049	0.2333

MACE-Osaka26 maintains high predictive accuracy and strong generalization capabilities even for highly complex, multi-component heavy-element ceramics.

### C. Lattice Thermal Conductivity

Finally, to demonstrate the applicability of MACE-Osaka26 to demanding thermal properties, we evaluated the lattice thermal conductivity ( $\kappa_L$ ) of actinide fluorite oxides. The calculations were performed by solving the phonon Wigner transport equation [63, 64], leveraging the second- and third-order interatomic force constants generated by the MACE-Osaka26 MLIP.

Figure 5(a) presents the predicted temperature dependence of  $\kappa_L$  for a comprehensive series of actinide dioxides ( $AnO_2$ , where  $An = \text{Th, Pa, U, Np, Pu, Am, Cm, and Cf}$ ). For systems where reference experimental data are available (such as  $UO_2$  [60],  $AmO_2$  [61],  $ThO_2$  [65],  $PuO_2$  [66–68],  $CmO_2$  [69] and  $NpO_2$  [70]), the absolute values are consistent with experimental reports across a wide temperature range (300–1500 K). It is particularly noteworthy that a single universal model successfully evaluated the thermal properties across this entire actinide series without yielding any imaginary phonon frequencies. The complete absence of imaginary modes across all eight distinct systems confirms the robust dynamical stability of the predicted structures and underscores the high physical fidelity of the learned anharmonic potential energy surface for heavy elements.

To investigate the impact of transuranium element doping—a critical scenario for advanced nuclear fuel engineering and waste transmutation—we extended this analysis to a mixed oxide system. The solid solution was systematically modeled by substituting one U atom with an Am atom within the 12-atom conventional fluorite unit cell ( $U_4O_8 \rightarrow U_3Am_1O_8$ ), yielding  $Am_{0.25}U_{0.75}O_2$ . Crucially, as shown in Figure 5(b), we compared these MLIP predictions against experimentally obtained lattice thermal conductivities for pure  $UO_2$  [60], pure  $AmO_2$  [61], and the  $Am_{0.20}U_{0.80}O_2$  [62] solid solution. Despite the slight difference in Am concentration dictated by the periodic boundary conditions of the unit cell (25% in the model versus 20% in the experiment), the MLIP quantitatively captures the severe degradation of thermal performance induced by Am doping, seamlessly bridging the properties of the two pure end-members.

## III. DISCUSSION

The superior performance of MACE-Osaka26, characterized by reduced outliers and improved stability in heavy element systems, is largely attributed to the increased graph cutoff radius. MACE-Osaka24 employed a shorter cutoff of 4.5 Å, which was previously reported to be insufficient for accurately describing heavy element BCC structures due to the limited neighbor lists (as dis-

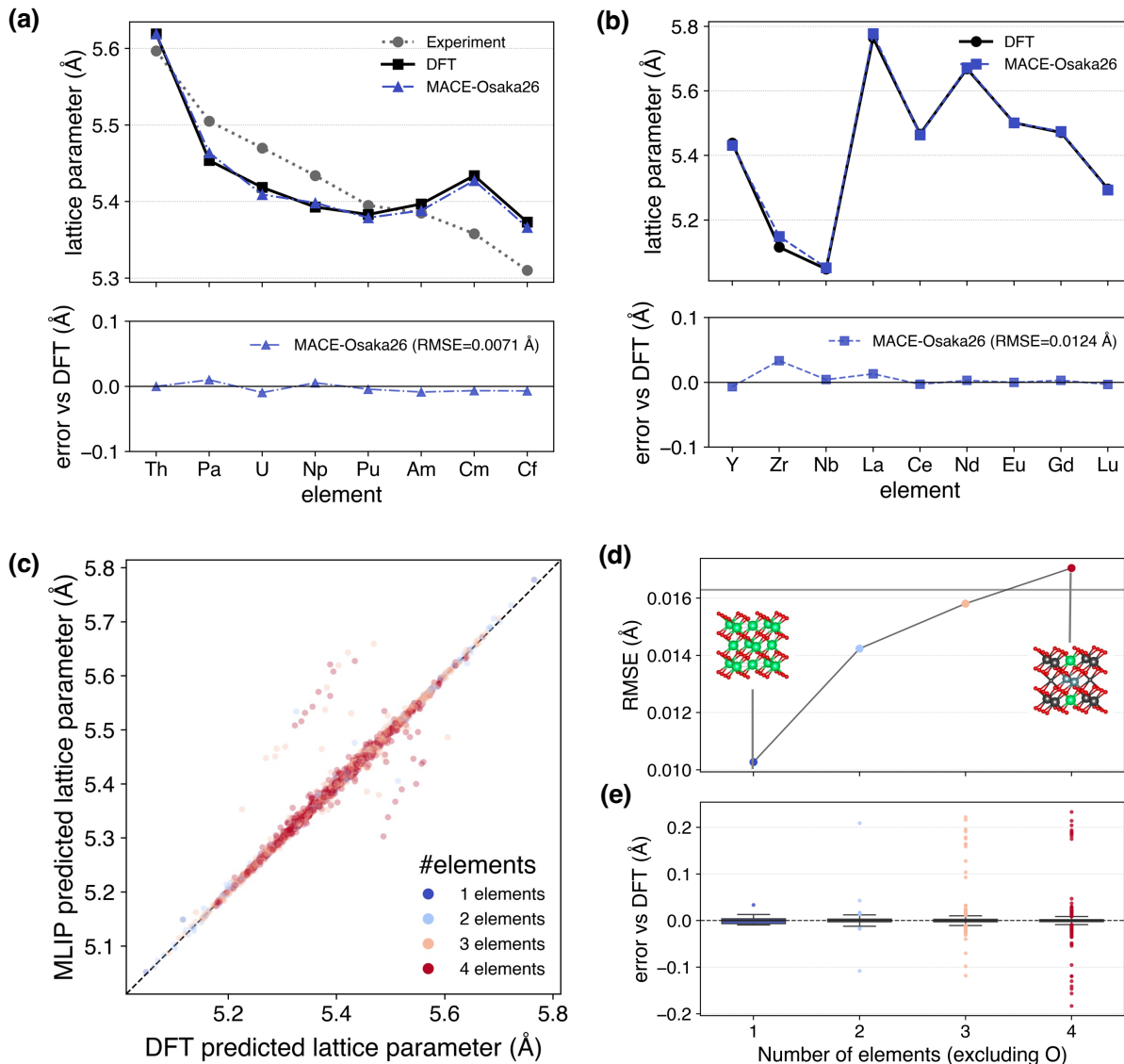


FIG. 4. Evaluation of MACE-Osaka26 on compositionally complex fluorite oxides. (a) Comparison of predicted lattice parameters with DFT reference values and experimental data across the actinide series (Th to Cf). The bottom panel shows the error of MACE-Osaka26 relative to DFT. (b) Predicted lattice parameters for fluorite-structured oxides containing various rare metals and lanthanides. (c) Parity plot of MLIP-predicted versus DFT-calculated lattice parameters, color-coded by the number of constituent elements (excluding oxygen). (d) Root-mean-square error (RMSE) and (e) error distribution relative to DFT as a function of the number of constituent elements.

cussed in the Appendix of Ref. [48]). By extending the cutoff to 6.0 Å in MACE-Osaka26, the model can capture longer-range interactions essential for these systems. This modification not only resolves the issues with heavy elements but also enhances the generalization capability across diverse chemical environments, including molecular systems (OFF23) and general crystalline structures (MPtrj).

The prediction accuracy for the lattice parameters of the BHE subset, which contains elemental solids and bi-

nary oxides, was found to be an order of magnitude lower than that of the CHE subset, which includes complex multi-component systems. This discrepancy is primarily attributed to the smaller sample size of the BHE subset (42 structures) compared to the CHE subset (136 structures), as well as the presence of specific outliers with errors approaching 1.0 Å. Except for a single case of Cf, the elements exhibiting large deviations are not included in the relatively larger CCFO subset, indicating a lower representation in the training data. These results sug-

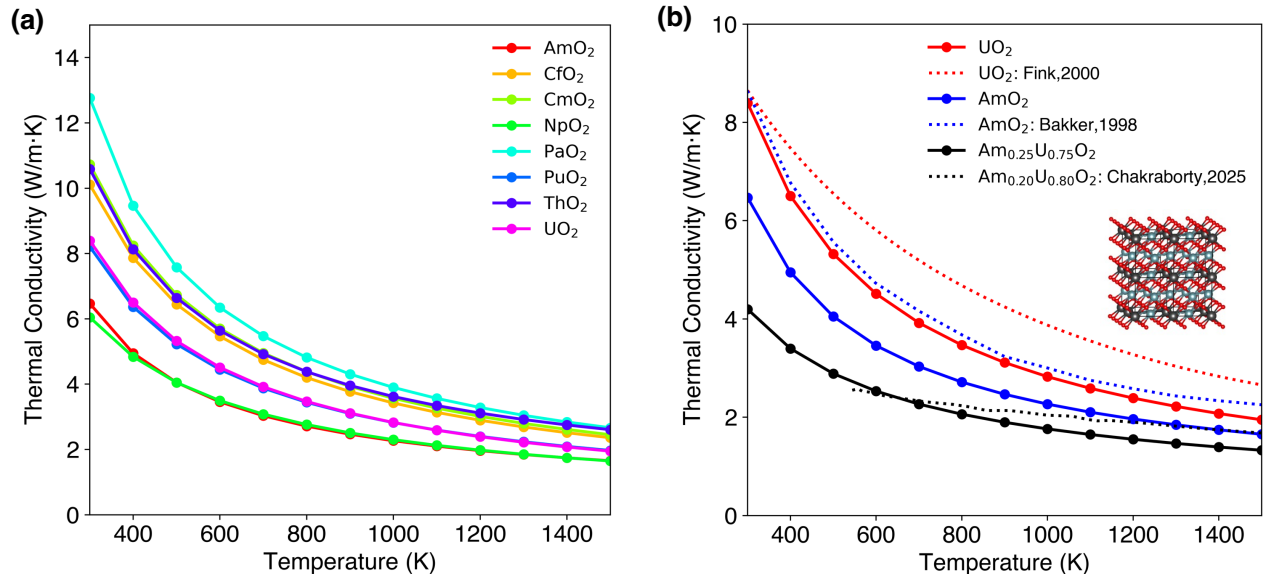


FIG. 5. Lattice thermal conductivity ( $\kappa_L$ ) of actinide oxides predicted by MACE-Osaka26. (a) Temperature dependence of  $\kappa_L$  for a series of actinide dioxides ( $AnO_2$ ,  $An = Th, Pa, U, Np, Pu, Am, Cm, Cf$ ). The solid lines with symbols represent the MLIP results calculated by solving the Wigner transport equation via phono3py, while the open symbols denote experimental data from the literature where available. (b) Comparison of  $\kappa_L$  between the pure binary oxides and the ternary solid solution Am<sub>0.25</sub>U<sub>0.75</sub>O<sub>2</sub>. The experimentally obtained lattice thermal conductivities for pure UO<sub>2</sub> [60], AmO<sub>2</sub> [61], and the solid solution Am<sub>0.2</sub>U<sub>0.8</sub>O<sub>2</sub> [62] are plotted as dotted curves to validate the MLIP predictions.

gest that further expansion of the dataset will likely lead to improvements in prediction accuracy for these heavy-element systems.

In the lattice thermal conductivity predictions for actinide FOs, the total absence of imaginary phonon modes across the entire actinide series is particularly significant, as it demonstrates the robust dynamical stability of the predicted structures and the high physical fidelity of the learned anharmonic potential energy surface. Furthermore, extracting third-order force constants for disordered systems typically requires extremely large supercells, making conventional DFT calculations computationally prohibitive. The ability of MACE-Osaka26 to efficiently and accurately model these thermophysical properties of actinide FOs indicates its suitability for the computational design of next-generation nuclear fuels.

#### IV. CONCLUSION

In this study, we constructed a heavy element first-principles calculation dataset HE26. Existing large-scale datasets such as MPtrj cover up to 89 elements, but for certain heavy elements outside this range, essentially no first-principles dataset has been available. HE26 fills this gap by explicitly including eight heavy elements (i.e., Am, Cm, Cf, Fr, At, Ra, Po, and Rn). The dataset spans elemental solids, binary oxides, multi-component compounds drawn from the literature and crystallographic databases, and compositionally complex

actinide-lanthanide fluorite-type solid solutions. By integrating HE26 with the molecular (OFF23) and crystalline (MPtrj) datasets through the total energy alignment (TEA) protocol, we developed MACE-Osaka26, a universal MLIP covering 97 elements. To the best of our knowledge, this is the broadest elemental coverage among existing MLIPs. The model and data are both publicly freely available, providing a reproducible starting point for building universal MLIPs that include heavy elements.

The resulting MACE-Osaka26 maintains accuracy and generalization across the molecular and crystalline domains. The model also stably reproduces property trends along structural scales and compositional series for the heavy element systems covered by HE26. Furthermore, we evaluated the lattice thermal conductivity of actinide fluorite oxides and their solid solutions. Second- and third-order interatomic force constants were generated with the MLIP, and the lattice thermal conductivity  $\kappa_L$  was obtained by solving the Wigner transport equation. The results agreed with reference experiments over a wide temperature range. For a transuranium-doped solid solution such as Am<sub>0.25</sub>U<sub>0.75</sub>O<sub>2</sub>, the model quantitatively captured the large reduction in thermal conductivity caused by Am doping. These results demonstrate that a universal MLIP can provide a scalable route to evaluating thermal transport properties of compositionally complex systems containing transuranium elements. Such evaluations have been not easy to carry out with first-principles calculations alone.

However, HE26 and MACE-Osaka26 represent only a first step towards accelerating computation in the heavy element regime. The reference electronic structures in this study are based on PBE (and partially DFT+U), chosen for compatibility with MPtrj. For transuranium element systems where strongly correlated  $f$ -electrons, magnetism, and spin-orbit coupling (SOC) are significant, the validity of the reference calculations itself can become a source of uncertainty. Going forward, it will be important to (i) generate datasets based on electronic structure calculations that include SOC, (ii) cross-check with higher-level electronic structure methods, (iii) expand external validation against experimental data (lattice constants, thermochemistry, elasticity, thermal transport), and (iv) strategically increase data through uncertainty quantification and active learning. Through these efforts, the reliability and scale of datasets covering transuranium elements should be improved step by step.

Today’s MLIPs have reached practical utility by starting from relatively small initial datasets and building up through continuous data expansion and validation. HE26 serves as a starting point for extending the same development path into the heavy element regime. Moreover, the intermediate features learned by universal MLIPs can serve as compact atomic descriptors for chemical properties beyond energy and its derivatives [71–75]. Extending these descriptors to 97 elements broadens the accessible chemical space for materials design and screening through materials informatics. In summary, this work may provide an open foundation for accelerating large-scale screening and property prediction of heavy elements in nuclear materials science, encompassing nuclear fuels, waste forms, and actinide-bearing high-entropy ceramics.

## V. METHODS

### A. HE26 Dataset

The HE26 dataset was generated using the Vienna *Ab initio* Simulation Package (VASP) [76–79] and extends the elemental coverage to eight heavy elements: Am, Cm, Cf, Fr, At, Ra, Po, and Rn. For actinide-containing systems, where electronic-structure convergence can be sensitive to magnetism, we first identified a suitable magnetic configuration via single-point calculations over multiple candidate magnetic states. Details of this magnetic-structure selection procedure are provided in Appendix A 1 b. Geometry optimizations were then performed starting from the selected configuration.

After the DFT calculations, we curated the raw HE26 structures to improve data quality and reduce noise during training. Specifically, we removed (i) structures whose geometry optimizations did not complete, (ii) structures with positive total energies for all elements except the noble gas Rn (to avoid spurious high-energy outliers), and (iii) structures for which the self-consistent field (SCF) iterations failed to converge during geometry

optimization.

In the following subsections, we describe the generation procedures for each HE26 subset: BHE, CHE, and CCFO.

#### 1. Basic Heavy Element Subset

For the elemental systems and binary oxides of eight heavy elements (Am, Cm, Cf, Fr, At, Ra, Po, and Rn), we compiled structural data using a stepwise approach. First, we utilized available Crystallographic Information File (CIF) formats from the Crystallography Open Database (COD) database [80, 81]. For structures not included in the COD, initial geometries were generated by searching the literature. Additionally, for basic crystal structures—specifically body-centered cubic (bcc), face-centered cubic (fcc), and hexagonal close-packed (hcp)—that could not be obtained from experimental values, initial geometries were generated using a same-volume approximation derived from the experimental values of other structures.

#### 2. Complex Heavy Element Subset

For the complex multi-element systems of eight heavy elements not found in the MPtrj dataset, we compiled structural data from multiple sources. First, we used available CIF files from the COD database. Any equivalent structures were excluded using `pymatgen’s StructureMatcher` [82], even if they possessed different COD ID. Additionally, for structures not registered in the COD database, we searched the literature as extensively as possible and prepared the corresponding initial structures. To further increase the number of structures, we retrieved additional structures from the Inorganic Substances Database book 2017 [83] that were not covered by the previous steps and generated their corresponding initial geometries.

#### 3. Compositionally Complex Fluorite Oxide Subset

The initial lattice constant of fluorite  $\text{Th}_4\text{O}_8$  (the conventional unit cell of fluorite  $\text{ThO}_2$ ) was obtained from MPtrj. Subsequently, initial structures prior to geometry optimization were generated for all combinations of 1–4 substitutions of Th with  $X \in \{\text{La, Ce, Nd, Eu, Gd, Lu, Y, Zr, Nb, Th, Pa, U, Np, Pu, Am, Cm, Cf}\}$ .  $\text{Th}_4\text{O}_8$  was selected as the parent cell because it possesses the largest lattice constant within the  $\text{AnO}_2$  ( $\text{An} = \text{Th, Pa, U, Np, Pu, Am, Cm, Cf}$ ) series [84–86]. Starting with the largest host lattice minimizes the risk of unphysically short interatomic distances in the initial substituted structures prior to relaxation. This approach ensures that the dataset robustly covers compositionally complex mixed oxides containing not only actinides but also

critical minor metal elements and transition metals. The actinide subset (Th, Pa, U, Np, Pu, Am, Cm, Cf) was chosen because stable bulk actinide dioxides crystallizing in the  $\text{CaF}_2$ -type (fluorite) structure have been experimentally established across this series [84]. Actinium was excluded because its chemistry is strongly dominated by the +III oxidation state, and a stable fluorite  $\text{AcO}_2$  phase has not been observed [87, 88]. To explicitly encompass rare-earth elements, yttrium (Y) and a representative lanthanide subset (La, Ce, Nd, Eu, Gd, Lu) were included. These rare-earth species are technologically critical as abundant nuclear fission products and common aliovalent dopants. They frequently form substituted fluorite solid solutions, such as  $\text{Y}_2\text{O}_3$ -doped  $\text{ThO}_2$  and various  $\text{UO}_2$ -based matrices. This selection systematically spans a broad range of ionic radii across the lanthanide contraction while simultaneously sampling diverse  $4f$ -electron configurations and redox flexibility [89–91]. Finally, transition-metal cations (Zr, Nb) were selected because fluorite-type actinide dioxide matrices commonly accommodate them as dopants or within macroscopic solid solutions. For instance,  $\text{UO}_2$ – $\text{ZrO}_2$  and  $\text{ThO}_2$ – $\text{ZrO}_2$  readily form extended fluorite solid solutions, and fluorite  $\text{UO}_2$  exhibits measurable Nb solubility upon  $\text{Nb}_2\text{O}_5$  addition [92–94].

## B. 97-element Universal Dataset

In Ref. [48], we integrated the MPtrj and OFF23 datasets using TEA protocol. It should be noted that the dispersion correction values were subtracted from the OFF23 dataset. Following the data splitting protocol established in Ref. [55] and Ref. [57], 95% of the MPtrj and OFF23 datasets were used for training and validation, while the remaining 5% were reserved for testing. The HE26 dataset was generated under conditions compatible with the MPtrj dataset, allowing for its direct integration into the MPtrj+OFF23 dataset. Although the HE26 dataset encompasses nearly all known experimentally synthesized crystal and complex structures, its volume is small compared to MPtrj and OFF23. Therefore, all data in HE26 were used for training and validation without a separate test split. In this study, the combined training and validation data are referred to as the “training set.” We designate this combined MPtrj+OFF23+HE26 dataset as the “97-element universal dataset.”

## C. MLIP Training

Using the 97-element universal dataset (MPtrj + OFF23 + HE26), we trained MLIPs with the MACE framework [40, 55], using mace v0.3.12 (<https://github.com/ACESuit/mace>). We denote the resulting MLIP as MACE-Osaka26. The model and the final training data are available at <https://github.com/>

[qiqb-osaka/mace-osaka26](#). Training followed the hyperparameters, cost functions, and optimizers of the MACE-MP-0 described in Ref. [55], with minor modifications. For this model, we set a cutoff radius of 6.0 Å for constructing the atomic neighborhood graph. We adopted the same atomic reference energies as MACE-MPA-0 for the 89 elements present in MPtrj, while calculating spin-polarized VASP energies for the isolated atoms of the eight newly added heavy elements. We incorporate a short-range repulsive correction via the Ziegler–Biersack–Littmark (ZBL) [95] screened nuclear potential and, to make it consistent across elements, apply an element-dependent Agnesi distance transformation [96] based on covalent radii before evaluating the radial basis. The model was trained using 32 NVIDIA A100 GPUs across 4 nodes on SQUID, the large-scale computing system at D3 Center, The University of Osaka.

## D. Lattice Thermal Conductivity Calculation

Although lattice thermal conductivity can in principle be evaluated using the Green–Kubo formalism, lattice thermal conductivity in crystalline solids arising from anharmonic phonon–phonon interactions can be computed more efficiently within a lattice-dynamics framework by solving phonon transport equations, such as the Peierls–Boltzmann transport equation (PBTE) or the Wigner transport equation (WTE) [63, 64, 97, 98]. The predictive accuracy of these approaches depends critically on the fidelity of the underlying interatomic forces. While empirical force fields are computationally efficient, their transferability is often limited, whereas first-principles calculations provide more accurate interatomic forces at a substantially higher computational cost. In particular, the calculation of third-order anharmonic interatomic force constants (IFCs) using DFT becomes a major bottleneck for multicomponent, low-symmetry, or defect-containing systems, because the required supercell sizes and the number of displaced configurations increase rapidly as the crystal symmetry is reduced [24]. To balance accuracy and computational efficiency, the lattice thermal conductivity ( $\kappa_L$ ) and phonon dispersion relations in this study were calculated using the finite displacement method implemented in the phono3py package [99, 100], with atomic forces evaluated using the trained MACE-Osaka26 potential.

For certain heavy elements (e.g., Am) whose default atomic masses are not registered in phono3py, standard atomic weights were specified manually. Prior to the phonon calculations, full geometry optimizations of all structural models were performed until the residual forces on each atom converged to less than 0.03 eV/Å.

For the pure actinide dioxides ( $\text{AnO}_2$ ), we adopted a supercell containing a total of 96 atoms, constructed by expanding the 12-atom fluorite conventional unit cell to  $2 \times 2 \times 2$ . The second- and third-order interatomic force

constants (IFCs) were extracted using a finite atomic displacement distance of 0.03 Å. To model the mixed oxide solid solution ( $\text{Am}_{0.25}\text{U}_{0.75}\text{O}_2$ ), one U atom within the 12-atom conventional unit cell was substituted with an Am atom ( $\text{U}_4\text{O}_8 \rightarrow \text{U}_3\text{Am}_1\text{O}_8$ ), which was subsequently expanded into a  $2 \times 2 \times 2$  supercell. In this mixed system, the reduction in symmetry leads to a massive proliferation in the number of force evaluations (displacement patterns) required to extract the third-order IFCs. Therefore, to keep the computational cost within a practical range, a cutoff radius of 6 Å was applied to the IFC calculations.

Crucially, the macroscopic heat transport was evaluated by solving the phonon Wigner transport equation rather than the conventional Peierls-Boltzmann transport equation (PBTE). Under this Wigner formalism—formulated by Simoncelli et al. and Isaeva et al. and implemented in `phono3py`—the total lattice thermal conductivity tensor  $\kappa_L^{\alpha\beta}$  is described as the sum of two components:

$$\kappa_L^{\alpha\beta} = \kappa_P^{\alpha\beta} + \kappa_C^{\alpha\beta} \quad (1)$$

Here,  $\alpha$  and  $\beta$  are subscripts denoting the Cartesian coordinate directions ( $x, y, z$ ). The first term,  $\kappa_P^{\alpha\beta}$ , originates from the diagonal elements of the heat flux operator and represents the conventional PBTE contribution (particle-like heat transport) governed by phonon group velocities and relaxation times. Conversely, the second term,  $\kappa_C^{\alpha\beta}$ , arises from the off-diagonal elements and captures the “wave-like coherent heat transport” (inter-band tunneling), reflecting the coupling between different phonon branches ( $j \neq j'$ ) with proximate angular frequencies. Incorporating this coherent component,  $\kappa_C^{\alpha\beta}$ , is theoretically indispensable for the low-symmetry  $\text{Am}_{0.25}\text{U}_{0.75}\text{O}_2$  supercell. Due to zone folding in this structure, optical phonon modes densely proliferate and intertwine, reducing the inter-band energy differences to a magnitude comparable to the phonon linewidths (scattering rates).

The macroscopic scalar lattice thermal conductivity,  $\kappa_L$ , reported in this study is defined as the average of the three diagonal components of the tensor:

$$\kappa_L = \frac{1}{3}(\kappa_L^{xx} + \kappa_L^{yy} + \kappa_L^{zz}) \quad (2)$$

The Brillouin zone integration for this evaluation was performed using a uniform  $10 \times 10 \times 10$   $q$ -point mesh. In the present calculations, isotope scattering was excluded to isolate and focus on the intrinsic anharmonic phonon-phonon scattering, as well as the point defect scattering originating from mass and force-constant variances in the mixed oxide system.

## ACKNOWLEDGMENTS

This project was supported by funding from the MEXT Quantum Leap Flagship Program (MEXT-QLEAP) through Grant No. JPMXS0120319794, the

JST COI-NEXT Program through Grant No. JPMJPF2014, and the JST ASPIRE Program Grant No. JPMJAP2319. The completion of this research was partially facilitated by the JSPS Grants-in-Aid for Scientific Research (KAKENHI), specifically Grant Nos. JP23H03819, and JP25K23358. We thank the Supercomputer Center, the Institute for Solid State Physics, the University of Tokyo, for allowing us to use their facilities. A part of the calculations were performed using the Genkai supercomputer of the Research Institute for Information Technology at Kyushu University. This work was also achieved using the SQUID supercomputer at the Cybermedia Center, The University of Osaka.

## Appendix A: Computational Details

### 1. Electronic-structure reference calculations

#### *a. General DFT Setting*

VASP calculations were performed using periodic boundary conditions and PAW pseudopotentials. Unless stated otherwise, the input settings followed the Materials Project-style defaults as implemented in `pymatgen’s MPRelaxSet` [82]. We applied specific explicit overrides across all calculations to ensure consistency with recent large-scale dataset practices (e.g., OMat24 [44]). Specifically, we utilized the normal electronic minimization algorithm (`ALGO = Normal`) and set the electronic self-consistency convergence criterion to  $10^{-5}$  eV (`EDIFF = 1e-05`). We applied Gaussian smearing (`ISMEAR = 0`) with a broadening width of 0.05 eV (`SIGMA = 0.05`), and the baseline charge density mixing parameters were set to `AMIX = 0.2` and `BMIX = 0.0001`. To improve computational efficiency and reduce I/O overhead, parallelization over bands was specified (`NPAR = 4`), and the writing of charge density and wavefunctions was suppressed (`LCHARG = .FALSE.`, `LWAVE = .FALSE.`). Other general parameters (e.g.,  $k$ -point meshes) were strictly inherited from the `MPRelaxSet` defaults.

As a consequence of these inherited defaults and explicit settings, the calculations employed a plane-wave energy cutoff of 520.0 eV (`ENCUT = 520.0`), “Accurate” precision (`PREC = Accurate`), and automatic real-space projection (`LREAL = Auto`). To ensure the accurate treatment of localized states, non-spherical contributions from the PAW spheres were included (`LASPH = .TRUE.`), and the maximum angular momentum for charge density mixing was set to `LMAXMIX = 6`. Furthermore, though the writing of charge density and wavefunctions was suppressed, DOS and band structure projection data were still calculated and written (`LORBIT = 11`). Finally, the maximum number of electronic steps (`NELM`) was set to 100, extending to 1000 if convergence was not initially reached.

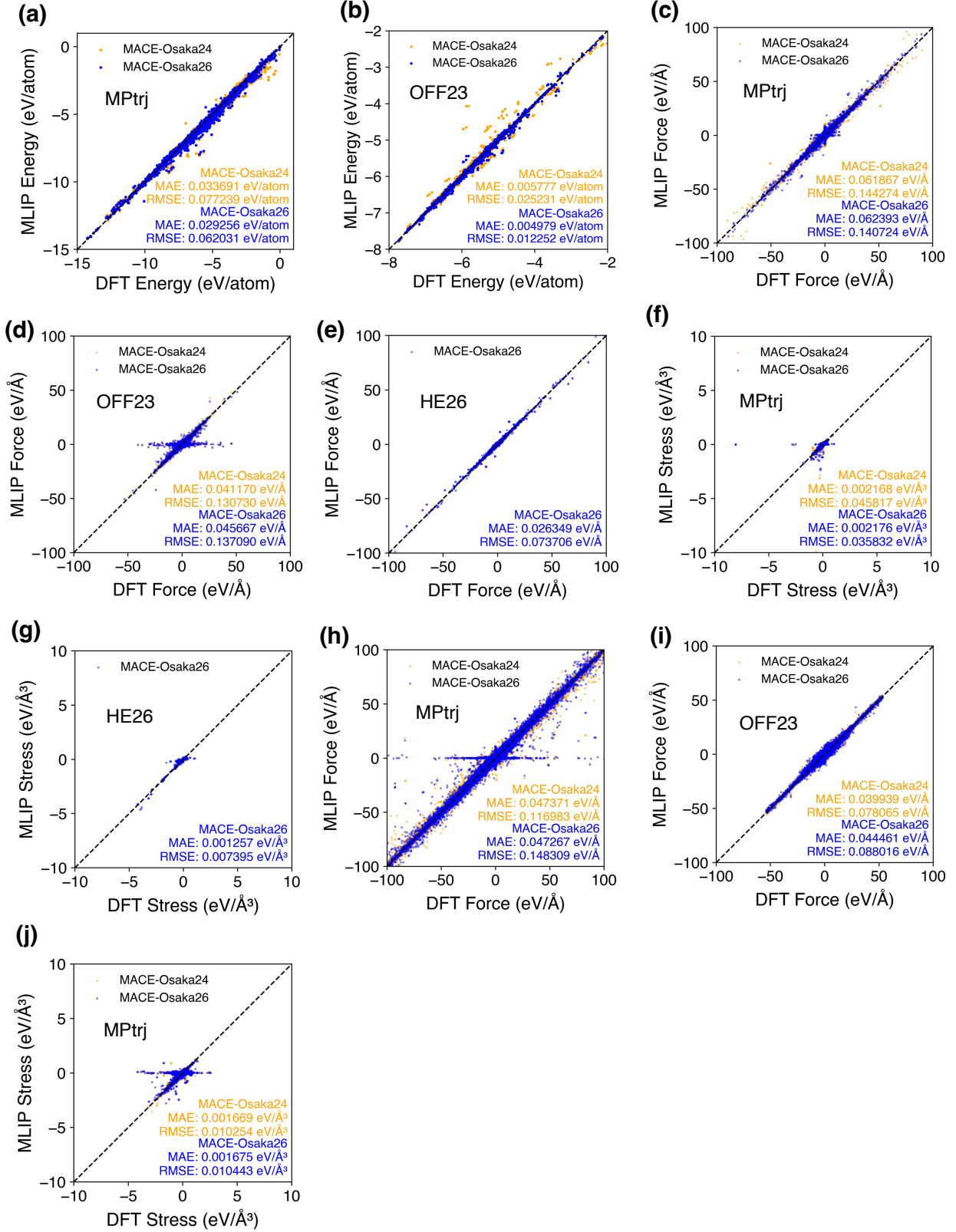


FIG. 6. Accuracy comparison of energies, atomic forces, and virial stresses between MACE-Osaka24 and MACE-Osaka26. (a, b) Parity plots for energies evaluated on (a) the MPtrj test set and (b) the OFF23 test set. (c–e) Parity plots for atomic forces evaluated on (c) the MPtrj test set, (d) the OFF23 test set, and (e) the Heavy (HE26) dataset. (f, g) Parity plots for virial stresses evaluated on (f) the MPtrj test set and (g) the Heavy (HE26) dataset. (h–j) Parity plots for training set evaluated for atomic forces on (h) the MPtrj test set and (i) the OFF23 test set, and for virial stresses on (j) the MPtrj test set. Note that for the Heavy (HE26) dataset where MACE-Osaka24 is not applicable or not supported, only the results for MACE-Osaka26 (blue) are shown. Mean absolute errors (MAE) and root-mean-square errors (RMSE) are provided in units of eV/atom for energies, eV/Å for forces, and eV/Å<sup>3</sup> for stresses.

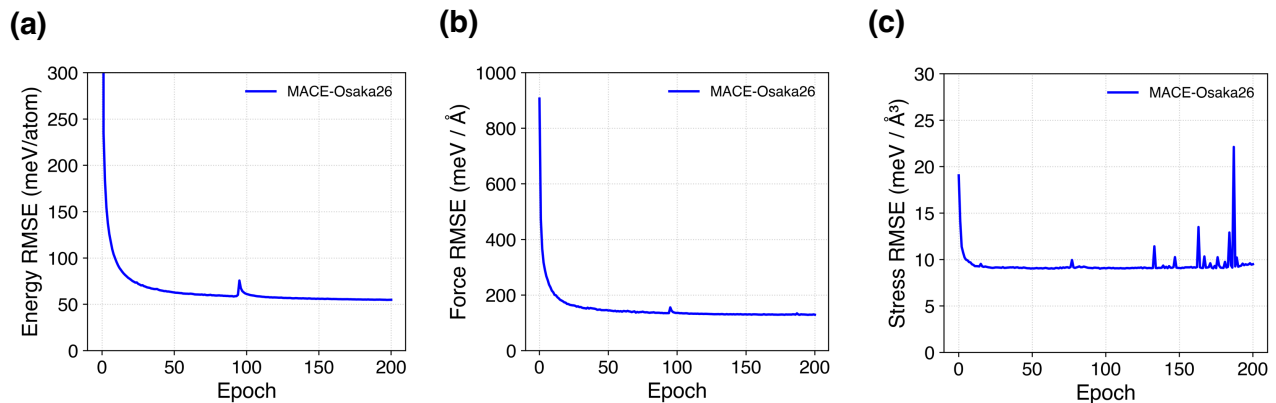


FIG. 7. Root mean square errors (RMSEs) obtained during training of the MACE-Osaka26 model for 200 epochs. (a) RMSE of the energy per atom (meV/atom). (b) RMSE of the forces (meV/Å). (c) RMSE of the stresses (meV/Å<sup>3</sup>).

### b. Magnetic-configuration screening

Various initial magnetic configurations were screened by single-point calculations at fixed ionic positions, explicitly disabling ionic relaxation by setting `IBRION = -1` and `NSW = 0`. The evaluated configurations included ferromagnetic (FM), antiferromagnetic (AFM), no spin, and the `pymatgen` default for the `MAGMOM` parameters (initial on-site magnetic moments of each atom). All other electronic minimization and I/O parameters followed the general settings described in Section A 1 a. The magnetic configuration used for subsequent geometry optimizations was selected using an automated decision rule based on the resulting energies and Self-Consistent Field (SCF) convergence behavior. Specifically, we (i) considered only calculations for which the electronic self-consistency cycle converged normally; (ii) identified the minimum-energy-per-atom solution, treated solutions within 10 meV/atom of this minimum as energetically degenerate, and selected from this degenerate set the configuration with the smallest SCF iteration count; (iii) if the preliminary selection required more than 200 SCF iterations, we allowed a fallback to an alternative configuration within 20 meV/atom whose SCF iteration count was reduced by at least 100, to improve robustness; and (iv) additionally performed a non-spin-polarized single-point calculation with `ISPIN = 1`, and if its energy per atom was within 10 meV/atom of the minimum-energy solution, we selected this non-magnetic state and, for subsequent structural relaxations, kept `ISPIN = 2` while initializing all site moments to zero (i.e., `MAGMOM = 0` for all atoms). Finally, when a spin-polarized configuration was selected, the site-resolved converged magnetic moments of that run were used as the initial `MAGMOM` for subsequent structural relaxations.

### c. Geometry optimization

Structural relaxations utilized the converged site-resolved magnetic moments from the initial screening step as the starting `MAGMOM` values. The geometry optimizations allowed for the full relaxation of atomic positions, cell shape, and volume (`ISIF = 3`) using the conjugate gradient algorithm (`IBRION = 2`). The maximum number of ionic steps (`NSW`) was initially set to 99; if convergence was not reached, this limit was extended to 1000 steps. The ionic convergence criterion was defined by a force threshold of `-0.03 eV/Å` (`EDIFFG = -0.03`). All other electronic and general parameters were inherited from Section A 1 a.

Exchange–correlation effects were treated within the generalized gradient approximation using the Perdew–Burke–Ernzerhof (PBE) functional. For oxide and fluoride materials containing Co, Cr, Fe, Mn, Mo, Ni, V, or W, Hubbard U corrections were applied following the Materials Project defaults (`pymatgen MPRelaxSet`).

## Appendix B: Benchmarking Force and Stress on Cross-domain Datasets

To complement the energy accuracy discussions in the main text, we provide a detailed evaluation of the total energies, atomic forces, and stresses predicted by MACE-Osaka26. Figure 6 displays the parity plots for these properties across the MPtrj, OFF23, and HE26 dataset. The results confirm that the model maintains high predictive performance for derivative physical quantities, ensuring its applicability to diverse tasks such as structural optimization and molecular dynamics simulations.

### Appendix C: Details of HE26 Dataset

Table III summarizes the information regarding the structural sources for the Basic Heavy Element (BHE) subset within the HE26 dataset. Tables IV and V outline the methods used for the structural sources of the Complex Heavy Element (CHE) subset.

### Appendix D: Training Curves of MACE-Osaka26

Figure 7 illustrates the evolution of validation accuracy for energy, forces, and stress during the 200-epoch

training of the MACE-Osaka26 model. As the number of epochs increases, the errors in energy and forces decrease smoothly. Regarding the stress component, although a significant transient increase is observed during training, the values eventually converge to a nearly constant level. Since this study focuses solely on training the model corresponding to MACE-Osaka24-small, it is expected that adopting hyperparameters consistent with the "large" version—as seen in MACE-Osaka24—would yield a smoother convergence curve for stress.

- 
- [1] D. C. Crawford, D. L. Porter, and S. L. Hayes, Fuels for sodium-cooled fast reactors: US perspective, *Journal of Nuclear Materials* **371**, 202 (2007).
  - [2] A. Magni, L. Luzzi, D. Pizzocri, A. Schubert, P. Van Uffelen, and A. Del Nevo, Modelling of thermal conductivity and melting behaviour of minor actinide-MOX fuels and assessment against experimental and molecular dynamics data, *Journal of Nuclear Materials* **557**, 153312 (2021).
  - [3] OECD Nuclear Energy Agency, *Homogeneous versus Heterogeneous Recycling of Transuranics in Fast Nuclear Reactors*, Tech. Rep. NEA No. 7077 (OECD Nuclear Energy Agency, Paris, France, 2012) © OECD 2012.
  - [4] T. Kooyman, Current state of partitioning and transmutation studies for advanced nuclear fuel cycles, *Annals of Nuclear Energy* **157**, 108239 (2021).
  - [5] OECD Nuclear Energy Agency, *Potential Benefits and Impacts of Advanced Nuclear Fuel Cycles with Actinide Partitioning and Transmutation*, Tech. Rep. NEA No. 6894 (OECD Nuclear Energy Agency, Paris, France, 2011).
  - [6] R. M. Ambrosi, E. J. Watkinson, A. Barco, R. Mesalam, T. Crawford, C. Bicknell, P. Samara-Ratna, D. Vernon, N. Bannister, D. Ross, J. Sykes, J. Byrne, B. Foxcroft, and H. Williams, European Radioisotope Thermoelectric Generators (RTGs) and Radioisotope Heater Units (RHUs) for Space Science and Exploration, *Space Science Reviews* **215**, 55 (2019).
  - [7] J. Brown, C. Campbell, C. Carrigan, M. Carrott, K. Greenough, C. Maher, B. McLuckie, C. Mason, C. Gregson, T. Griffiths, J. Holt, M. Sarsfield, K. Stephenson, R. Taylor, and T. Tinsley, Americium and plutonium purification by extraction (the AMPPEX process): Development of a new method to separate  $^{241}\text{Am}$  from aged plutonium dioxide for use in space power systems, *Progress in Nuclear Energy* **106**, 396 (2018).
  - [8] E. J. Watkinson, R. Mesalam, J.-F. Vigier, O. Beneš, J.-C. Griveau, E. Colineau, M. Sierig, D. Freis, R. M. Ambrosi, D. Staicu, and R. J. M. Konings, Thermal properties and behaviour of Am-bearing fuel in space radioisotope power systems, *Thermo* **1**, 297 (2021).
  - [9] T. Z. Ward, R. P. Wilkerson, B. L. Musicó, A. Foley, M. Brahlek, W. J. Weber, K. E. Sickafus, and A. R. Mazza, High entropy ceramics for applications in extreme environments, *Journal of Physics: Materials* **7**, 021001 (2024).
  - [10] K. Yang, K. Bryce, W. Zhu, D. Zhao, and J. Lian, Multicomponent pyrochlore solid solutions with uranium incorporation – a new perspective of materials design for nuclear applications, *Journal of the European Ceramic Society* **41**, 2870 (2021).
  - [11] Z. Liu, L. Wang, C. Ding, M. Tang, H. Xie, T. Li, X. Chen, Y. Ding, and J. Shi, Structural evolution and chemical durability of uranium-doped high-entropy pyrochlore, *Ceramics International* **50**, 5955 (2024).
  - [12] K. Minato, M. Takano, H. Otobe, T. Nishi, M. Akabori, and Y. Arai, Thermochemical and thermophysical properties of minor actinide compounds, *Journal of nuclear materials* **389**, 23 (2009).
  - [13] I. C. Njifon and E. Torres, Phonons and thermophysical properties of  $\text{U}_{1-y}\text{Pu}_y\text{O}_2$  mixed oxide (MOX) fuels, *Journal of Nuclear Materials* **537**, 152158 (2020).
  - [14] L. Bonatti, S. Middlemas, C. A. Hirst, and A. Navrotsky, Smaller and faster: a review of conventional and nanocalorimetry techniques for determining thermophysical properties of nuclear materials, *Journal of Thermal Analysis and Calorimetry* **150**, 13871 (2025).
  - [15] J. J. Carbajo, G. L. Yoder, S. G. Popov, and V. K. Ivanov, A review of the thermophysical properties of MOX and  $\text{UO}_2$  fuels, *Journal of Nuclear Materials* **299**, 181 (2001).
  - [16] R. J. M. Konings, L. R. Morss, and J. Fuger, Thermodynamic Properties of Actinides and Actinide Compounds, in *The Chemistry of the Actinide and Transactinide Elements*, edited by L. R. Morss, N. M. Edelstein, and J. Fuger (Springer Netherlands, Dordrecht, 2006) pp. 2113–2224.
  - [17] T. Uchida, T. Arima, K. Idemitsu, and Y. Inagaki, Thermal conductivities of americium dioxide and sesquioxide by molecular dynamics simulations, *Computational Materials Science* **45**, 229 (2009).
  - [18] V. Sobolev, Thermophysical properties of  $\text{NpO}_2$ ,  $\text{AmO}_2$  and  $\text{CmO}_2$ , *Journal of Nuclear Materials* **389**, 45 (2009), thermochemistry and Thermophysics of Nuclear Materials.
  - [19] D. H. Hurley, A. El-Azab, M. S. Bryan, M. W. D. Cooper, C. A. Dennett, K. Gofryk, L. He, M. Khafizov, G. H. Lander, M. E. Manley, J. M. Mann, C. A.

- Marianetti, K. Rickert, F. A. Selim, M. R. Tonks, and J. P. Wharry, Thermal energy transport in oxide nuclear fuel, *Chemical Reviews* **122**, 3711 (2022).
- [20] R. Woodley, The viscosity of molten uranium dioxide, *Journal of Nuclear Materials* **50**, 103 (1974).
- [21] A. Smith, Structure-property relationships in actinide containing molten salts – A review: Understanding and modelling the chemistry of nuclear fuel salts, *Journal of Molecular Liquids* **360**, 119426 (2022).
- [22] O. Y. Tkacheva, A. V. Rudenko, and A. A. Kataev, Viscosity of fluoride melts promising for molten salt nuclear reactors, *Electrochemical Materials and Technologies*. 2023. Vol. 2.№ 4 **2**, 10.15826/elmattech.2023.2.024 (2023).
- [23] Y. Yin, W. Liang, S. Shui, W. Zhou, and D. Wang, Physicochemical Properties and Structure of FLiBeTh Salts: Insights from Machine Learning Accelerated Molecular Dynamics Simulations, *The Journal of Physical Chemistry B* **129**, 10429 (2025), pMID: 41002787.
- [24] A. Togo, First-principles Phonon Calculations with Phonopy and Phono3py, *Journal of the Physical Society of Japan* **92**, 012001 (2023).
- [25] J. Behler and M. Parrinello, Generalized Neural-Network Representation of High-Dimensional Potential-Energy Surfaces, *Physical Review Letters* **98**, 146401 (2007).
- [26] A. P. Bartók, M. C. Payne, R. Kondor, and G. Csányi, Gaussian Approximation Potentials: The Accuracy of Quantum Mechanics, without the Electrons, *Physical Review Letters* **104**, 136403 (2010).
- [27] L. Zhang, J. Han, H. Wang, R. Car, and W. E, Deep Potential Molecular Dynamics: A Scalable Model with the Accuracy of Quantum Mechanics, *Physical Review Letters* **120**, 143001 (2018).
- [28] R. Jacobs, D. Morgan, S. Attarian, J. Meng, C. Shen, Z. Wu, C. Y. Xie, J. H. Yang, N. Artrith, B. Blaiszik, *et al.*, A practical guide to machine learning interatomic potentials—Status and future, *Current Opinion in Solid State and Materials Science* **35**, 101214 (2025).
- [29] A. V. Shapeev, Moment Tensor Potentials: A Class of Systematically Improvable Interatomic Potentials, *Multiscale Modeling & Simulation* **14**, 1153 (2016).
- [30] R. Drautz, Atomic cluster expansion for accurate and transferable interatomic potentials, *Physical Review B* **99**, 014104 (2019).
- [31] E. Stippell, L. Alzate-Vargas, K. N. Subedi, R. M. Tutchtón, M. W. D. Cooper, S. Tretiak, T. Gibson, and R. A. Messerly, Building a DFT+U machine learning interatomic potential for uranium dioxide, *Artificial Intelligence Chemistry* **2**, 100042 (2024).
- [32] E. T. Dubois, J. Tranchida, J. Bouchet, and J.-B. Maillet, Atomistic simulations of nuclear fuel UO<sub>2</sub> with machine learning interatomic potentials, *Physical Review Materials* **8**, 025402 (2024).
- [33] K. Kobayashi, M. Okumura, H. Nakamura, M. Itakura, M. Machida, and M. W. D. Cooper, Machine learning molecular dynamics simulations toward exploration of high-temperature properties of nuclear fuel materials: case study of thorium dioxide, *Scientific Reports* **12**, 9808 (2022).
- [34] L. Alzate-Vargas, K. N. Subedi, N. Lubbers, M. W. D. Cooper, R. M. Tutchtón, T. Gibson, and R. A. Messerly, Toward machine learning interatomic potentials for modeling uranium mononitride, *Machine Learning: Science and Technology* **6**, 035064 (2025).
- [35] J. Zhong, L. Zhang, and T. Bo, Active learning-enhanced neuroevolution potential for predictive modeling of UO<sub>2</sub> thermophysical properties, *Physical Chemistry Chemical Physics* **28**, 671 (2026).
- [36] E. Minamitani, M. Ogura, and S. Watanabe, Simulating lattice thermal conductivity in semiconducting materials using high-dimensional neural network potential, *Applied Physics Express* **12**, 095001 (2019).
- [37] K. T. Schütt, H. E. Sauceda, P.-J. Kindermans, A. Tkatchenko, and K.-R. Müller, SchNet—a deep learning architecture for molecules and materials, *The Journal of Chemical Physics* **148** (2018).
- [38] S. Batzner, A. Musaelian, L. Sun, M. Geiger, J. P. Mailoa, M. Kornbluth, N. Molinari, T. E. Smidt, and B. Kozinsky, E(3)-equivariant graph neural networks for data-efficient and accurate interatomic potentials, *Nature Communications* **13**, 2453 (2022).
- [39] A. Musaelian, S. Batzner, A. Johansson, L. Sun, C. J. Owen, M. Kornbluth, and B. Kozinsky, Learning local equivariant representations for large-scale atomistic dynamics, *Nature Communications* **14**, 579 (2023).
- [40] I. Batatia, D. P. Kovács, G. N. C. Simm, C. Ortner, and G. Csányi, Mace: Higher order equivariant message passing neural networks for fast and accurate force fields, in *Advances in Neural Information Processing Systems*, Vol. 35, edited by S. Koyejo, S. Mohamed, A. Agarwal, D. Belgrave, K. Cho, and A. Oh (Curran Associates, Inc., 2022) pp. 11423–11436, neurIPS 2022, arXiv:2206.07697.
- [41] Y. Park, J. Kim, S. Hwang, and S. Han, Scalable Parallel Algorithm for Graph Neural Network Interatomic Potentials in Molecular Dynamics Simulations, *Journal of Chemical Theory and Computation* **20**, 4857 (2024).
- [42] Y. Zhang and H. Guo, Node-equivariant message passing for efficient and accurate machine learning interatomic potentials, *Chem. Sci.* **17**, 3793 (2026).
- [43] B. Deng, P. Zhong, K. Jun, J. Riebesell, K. Han, C. J. Bartel, and G. Ceder, Chgnet as a pretrained universal neural network potential for charge-informed atomistic modelling, *Nature Machine Intelligence* **5**, 1031 (2023).
- [44] L. Barroso-Luque, M. Shuaibi, X. Fu, B. M. Wood, M. Dzamba, M. Gao, A. Rizvi, C. L. Zitnick, and Z. W. Ulissi, Open materials 2024 (omat24) inorganic materials dataset and models (2024), arXiv:2410.12771 [cond-mat.mtrl-sci].
- [45] J. Schmidt, H.-C. Wang, T. F. Cerqueira, S. Botti, and M. A. Marques, A dataset of 175k stable and metastable materials calculated with the pbesol and scan functionals, *Scientific Data* **9**, 64 (2022).
- [46] J. Schmidt, T. F. Cerqueira, A. H. Romero, A. Loew, F. Jäger, H.-C. Wang, S. Botti, and M. A. Marques, Improving machine-learning models in materials science through large datasets, *Materials Today Physics* **48**, 101560 (2024).
- [47] A. Mazitov, S. Chorna, G. Fraux, M. Bercx, G. Pizzi, S. De, and M. Ceriotti, Massive atomic diversity: a compact universal dataset for atomistic machine learning, *Scientific Data* **12**, 1857 (2025).
- [48] T. Shiota, K. Ishihara, T. M. Do, T. Mori, and W. Mizukami, Taming multi-domain, multi-fidelity data: Towards foundation models for atomistic scale simulations (2025), arXiv:2412.13088 [cond-mat.mtrl-sci].

- [49] B. M. Wood, M. Dzamba, X. Fu, M. Gao, M. Shuaibi, L. Barroso-Luque, K. Abdelmaqsood, V. Gharakhanyan, J. R. Kitchin, D. S. Levine, K. Michel, A. Sriram, T. Cohen, A. Das, A. Rizvi, S. J. Sahoo, Z. W. Ulissi, and C. L. Zitnick, UMA: A Family of Universal Models for Atoms (2025), arXiv:2506.23971 [cs.LG].
- [50] I. Batatia, C. Lin, J. Hart, E. Kesoar, A. M. Elena, S. W. Norwood, T. Wolf, and G. Csányi, Cross Learning between Electronic Structure Theories for Unifying Molecular, Surface, and Inorganic Crystal Foundation Force Fields (2025), arXiv:2510.25380 [physics.chem-ph].
- [51] S. Takamoto, C. Shinagawa, D. Motoki, K. Nakago, W. Li, I. Kurata, T. Watanabe, Y. Yayama, H. Iriguchi, Y. Asano, *et al.*, Towards universal neural network potential for material discovery applicable to arbitrary combination of 45 elements, *Nature Communications* **13**, 2991 (2022).
- [52] K. Nomura, S. Hattori, S. Ohmura, I. Kanemasu, K. Shimamura, N. Dasgupta, A. Nakano, R. K. Kalia, and P. Vashishta, Allegro-FM: Toward an Equivariant Foundation Model for Exascale Molecular Dynamics Simulations, *The Journal of Physical Chemistry Letters* **16**, 6637 (2025).
- [53] J. Kim, J. You, Y. Park, Y. Lim, Y. Kang, J. Kim, H. Jeon, S. Ju, D. Hong, S. Y. Lee, S. Choi, Y. Kim, J. W. Lee, and S. Han, Optimizing Cross-Domain Transfer for Universal Machine Learning Interatomic Potentials (2025), arXiv:2510.11241 [cond-mat.mtrl-sci].
- [54] T. Liang, K. Xu, E. Lindgren, Z. Chen, R. Zhao, J. Liu, E. Berger, B. Tang, B. Zhang, Y. Wang, K. Song, P. Ying, N. Xu, H. Dong, S. Chen, P. Erhart, Z. Fan, T. Ala-Nissila, and J. Xu, NEP89: Universal neuroevolution potential for inorganic and organic materials across 89 elements (2025), arXiv:2504.21286 [cond-mat.mtrl-sci].
- [55] I. Batatia, P. Benner, Y. Chiang, A. M. Elena, D. P. Kovács, J. Riebesell, X. R. Advincula, M. Asta, M. Avaylon, W. J. Baldwin, *et al.*, A foundation model for atomistic materials chemistry, *The Journal of Chemical Physics* **163**, 184110 (2025).
- [56] A. Jain, S. P. Ong, G. Hautier, W. Chen, W. D. Richards, S. Dacek, S. Cholia, D. Gunter, D. Skinner, G. Ceder, and K. A. Persson, Commentary: The materials project: A materials genome approach to accelerating materials innovation, *APL Materials* **1**, 011002 (2013).
- [57] D. P. Kovács, J. H. Moore, N. J. Browning, I. Batatia, J. T. Horton, Y. Pu, V. Kapil, W. C. Witt, I.-B. Magdau, D. J. Cole, *et al.*, Mace-off: Short-range transferable machine learning force fields for organic molecules, *Journal of the American Chemical Society* **147**, 17598 (2025).
- [58] C. Xu, T. Liu, Q. Liu, S. Yang, D. Li, and G. Tian, Complexation of Am (III) and Eu (III) with DRAPA (n, n-dialkyl-6-amide-pyridine-2-carboxylic acid), *Dalton Transactions* **52**, 15669 (2023).
- [59] J. Peterson and J. H. Burns, Preparation and crystal structure of californium oxyfluoride, CfOF, *Journal of Inorganic and Nuclear Chemistry* **30**, 2955 (1968).
- [60] J. K. Fink, Thermophysical properties of uranium dioxide, *Journal of Nuclear Materials* **279**, 1 (2000).
- [61] K. Bakker and R. Konings, On the thermal conductivity of inert-matrix fuels containing americium oxide, *Journal of Nuclear Materials* **254**, 129 (1998).
- [62] A. Chakraborty, P. Ghosh, N. Choudhury, and A. Arya, Thermal and diffusional properties of uranium-amerium and plutonium-amerium mixed oxides, *Journal of Nuclear Materials*, 156152 (2025).
- [63] M. Simoncelli, N. Marzari, and F. Mauri, Unified theory of thermal transport in crystals and glasses, *Nature Physics* **15**, 809 (2019).
- [64] M. Simoncelli, N. Marzari, and F. Mauri, Wigner formulation of thermal transport in solids, *Phys. Rev. X* **12**, 041011 (2022).
- [65] L. Malakkal, A. Prasad, E. Jossou, J. Ranasinghe, B. Szpunar, L. Bichler, and J. Szpunar, Thermal conductivity of bulk and porous ThO<sub>2</sub>: Atomistic and experimental study, *Journal of Alloys and Compounds* **798**, 507 (2019).
- [66] B.-T. Wang, J.-J. Zheng, X. Qu, W.-D. Li, and P. Zhang, Thermal conductivity of UO<sub>2</sub> and PuO<sub>2</sub> from first-principles, *Journal of Alloys and Compounds* **628**, 267 (2015).
- [67] C. Cozzo, D. Staicu, J. Somers, A. Fernandez, and R. Konings, Thermal diffusivity and conductivity of thorium-plutonium mixed oxides, *Journal of Nuclear Materials* **416**, 135 (2011).
- [68] R. L. Gibby, The effect of plutonium content on the thermal conductivity of (U, Pu) O<sub>2</sub> solid solutions, *Journal of Nuclear Materials* **38**, 163 (1971).
- [69] R. Konings, Thermochemical and thermophysical properties of curium and its oxides, *Journal of nuclear materials* **298**, 255 (2001).
- [70] T. Nishi, A. Itoh, M. Takano, M. Numata, M. Akabori, Y. Arai, and K. Minato, Thermal conductivity of neptunium dioxide, *Journal of nuclear materials* **376**, 78 (2008).
- [71] T. Shiota, K. Ishihara, and W. Mizukami, Universal neural network potentials as descriptors: towards scalable chemical property prediction using quantum and classical computers, *Digital Discovery* **3**, 1714 (2024).
- [72] A. El-Samman, S. De Castro, B. Morton, and S. De Baerdemacker, Transfer learning graph representations of molecules for pka, <sup>13</sup>C-nmr, and solubility, *Canadian Journal of Chemistry* **102**, 275 (2024).
- [73] R. A. Gouvêa, P.-P. De Breuck, T. Pretto, G.-M. Rignanese, and M. J. L. Santos, Combining feature-based approaches with graph neural networks and symbolic regression for synergistic performance and interpretability, *npj Computational Materials* <https://doi.org/10.1038/s41524-025-01938-2> (2026).
- [74] S. Y. Kim, Y. J. Park, and J. Li, Leveraging neural network interatomic potentials for a foundation model of chemistry, arXiv preprint arXiv:2506.18497 10.48550/arXiv.2506.18497 (2025).
- [75] M. Bojan, S. Vedula, S. A. Maddipatla, N. Bojan, A. Rzaev, F. Napoli, P. Schanda, and A. Bronstein, Representing local protein environments with machine learning force fields, in *The Fourteenth International Conference on Learning Representations* (2026).
- [76] G. Kresse and J. Hafner, Ab initio molecular dynamics for liquid metals, *Physical Review B* **47**, 558 (1993).
- [77] G. Kresse and J. Furthmüller, Efficient iterative schemes for ab initio total-energy calculations using a plane-wave basis set, *Physical Review B* **54**, 11169 (1996).

- [78] G. Kresse and J. Hafner, Ab initio molecular-dynamics simulation of the liquid-metal–amorphous-semiconductor transition in germanium, *Physical Review B* **49**, 14251 (1994).
- [79] G. Kresse and J. Furthmüller, Efficiency of ab-initio total energy calculations for metals and semiconductors using a plane-wave basis set, *Computational Materials Science* **6**, 15 (1996).
- [80] S. Gražulis, D. Chateigner, R. T. Downs, A. F. T. Yokochi, M. Quirós, L. Lutterotti, E. Manakova, J. Butkus, P. Moeck, and A. Le Bail, Crystallography Open Database – an open-access collection of crystal structures, *Journal of Applied Crystallography* **42**, 726 (2009).
- [81] S. Gražulis, A. Daškevič, A. Merkys, D. Chateigner, L. Lutterotti, M. Quirós, N. R. Serebryanaya, P. Moeck, R. T. Downs, and A. Le Bail, Crystallography Open Database (COD): an open-access collection of crystal structures and platform for world-wide collaboration, *Nucleic Acids Research* **40**, D420 (2012).
- [82] S. P. Ong, W. D. Richards, A. Jain, G. Hautier, M. Kocher, S. Cholia, D. Gunter, V. L. Chevrier, K. A. Persson, and G. Ceder, Python Materials Genomics (pymatgen): A robust, open-source python library for materials analysis, *Computational Materials Science* **68**, 314 (2013).
- [83] P. Villars, K. Cenzual, and R. Gladyshevskii, 2. Handbook of Inorganic Substances 2017 : References, in *Handbook* (De Gruyter, Berlin, Boston, 2017) pp. 1671–1956.
- [84] I. D. Prodan, G. E. Scuseria, and R. L. Martin, Covalency in the actinide dioxides: Systematic study of the electronic properties using screened hybrid density functional theory, *Phys. Rev. B* **76**, 033101 (2007).
- [85] U. Benedict, Structural data of the actinide elements and of their binary compounds with non-metallic elements, *J. Less-Common Met.* **128**, 7 (1987).
- [86] G. Wang, E. R. Batista, and P. Yang, Water on Actinide Dioxide Surfaces: A Review of Recent Progress, *Appl. Sci.* **10**, 4655 (2020).
- [87] G. J.-P. Deblonde, M. Zavarin, and A. B. Kersting, The coordination properties and ionic radius of actinium: A 120-year-old enigma, *Coord. Chem. Rev.* **446**, 214130 (2021).
- [88] S. Fried, F. Hagemann, and W. H. Zachariasen, The preparation and identification of some pure actinium compounds, *J. Am. Chem. Soc.* **72**, 771 (1950).
- [89] V. L. Vinograd, A. A. Bukaemskiy, G. Modolo, G. Deissmann, and D. Bosbach, Thermodynamic and Structural Modelling of Non-Stoichiometric Ln-Doped UO<sub>2</sub> Solid Solutions, Ln = La, Pr, Nd, Gd, *Frontiers in Chemistry* **9**, 705024 (2021).
- [90] H. S. Kim, C. Y. Joung, B. H. Lee, J. Y. Oh, Y. H. Koo, and P. Heimgartner, Applicability of CeO<sub>2</sub> as a surrogate for PuO<sub>2</sub> in a MOX fuel development, *Journal of Nuclear Materials* **378**, 98 (2008).
- [91] V. Alexandrov, N. Grønbech-Jensen, A. Navrotsky, and M. Asta, First-principles computational study of defect clustering in solid solutions of ThO<sub>2</sub> with trivalent oxides, *Phys. Rev. B* **82**, 174115 (2010).
- [92] D. Staicu, J. Somers, A. Fernandez, and R. Konings, Thermal properties of minor actinide targets, *Nuclear Materials and Energy* **3-4**, 6 (2015).
- [93] L. Zhang, A. Shelyug, and A. Navrotsky, Thermochemistry of UO<sub>2</sub>–ThO<sub>2</sub> and UO<sub>2</sub>–ZrO<sub>2</sub> fluorite solid solutions, *The Journal of Chemical Thermodynamics* **114**, 48 (2017).
- [94] Y. Harada, Sintering behaviour of niobia-doped large grain UO<sub>2</sub> pellet, *J. Nucl. Mater.* **238**, 237 (1996).
- [95] J. F. Ziegler and J. P. Biersack, The stopping and range of ions in matter, in *Treatise on heavy-ion science: volume 6: astrophysics, chemistry, and condensed matter* (Springer, 1985) pp. 93–129.
- [96] W. C. Witt, C. van der Oord, E. Gelžinytė, T. Järvinen, A. Ross, J. P. Darby, C. H. Ho, W. J. Baldwin, M. Sachs, J. R. Kermode, N. Bernstein, G. Csányi, and C. Ortner, Acepotentials.jl: A julia implementation of the atomic cluster expansion, *The Journal of Chemical Physics* **159**, 164101 (2023).
- [97] M. S. Green, Markoff Random Processes and the Statistical Mechanics of Time-Dependent Phenomena. II. Irreversible Processes in Fluids, *Journal of Chemical Physics* **22**, 398 (1954).
- [98] R. Kubo, Statistical-Mechanical Theory of Irreversible Processes. i. General Theory and Simple Applications to Magnetic and Conduction Problems, *Journal of the Physical Society of Japan* **12**, 570 (1957).
- [99] A. Togo, L. Chaput, and I. Tanaka, Distributions of phonon lifetimes in brillouin zones, *Phys. Rev. B* **91**, 094306 (2015).
- [100] A. Togo, L. Chaput, T. Tadano, and I. Tanaka, Implementation strategies in phonopy and phono3py, *J. Phys. Condens. Matter* **35**, 353001 (2023).
- [101] R. Wyckoff, Crystal structures 1 (7–83), *American Mineralogist Crystal Structure Database* **2** (1963).
- [102] S. Heathman, R. Haire, T. Le Bihan, A. Lindbaum, K. Litfin, Y. Méresse, and H. Libotte, Pressure Induces Major Changes in the Nature of Americium’s 5f Electrons, *Physical Review Letters* **85**, 2961 (2000).
- [103] D. Horlait, R. Caraballo, F. Lebreton, C. Jégou, P. Roussel, and T. Delahaye, Self-irradiation and oxidation effects on americium sesquioxide and raman spectroscopy studies of americium oxides, *Journal of Solid State Chemistry* **217**, 159 (2014).
- [104] D. Templeton and C. H. Dauben, Crystal Structures of Americium Compounds<sup>1</sup>, *Journal of the American Chemical Society* **75**, 4560 (1953).
- [105] A. Hermann, R. Hoffmann, and N. Ashcroft, Condensed astatine: monatomic and metallic, *Physical Review Letters* **111**, 116404 (2013).
- [106] S. Heathman, T. Le Bihan, S. Yagoubi, B. Johansson, and R. Ahuja, Structural investigation of californium under pressure, *Physical Review B—Condensed Matter and Materials Physics* **87**, 214111 (2013).
- [107] L. Petit, A. Svane, Z. Szotek, W. M. Temmerman, and G. M. Stocks, Electronic structure and ionicity of actinide oxides from first principles, *Phys. Rev. B* **81**, 045108 (2010).
- [108] R. Baybarz, R. Haire, and J. Fahey, On the californium oxide system, *Journal of Inorganic and Nuclear Chemistry* **34**, 557 (1972).
- [109] J. Stevenson and J. Peterson, Preparation and structural studies of elemental curium-248 and the nitrides of curium-248 and berkelium-249, *Journal of the Less Common Metals* **66**, 201 (1979).
- [110] H. O. Haug, Curium sesquioxide cm<sub>2</sub>o<sub>3</sub>, *Journal of Inorganic and Nuclear Chemistry* **29**, 2753 (1967).

- [111] A. Seleznev, V. Radchenko, V. Shushakov, M. Ryabinin, R. Droznic, L. Lebedeva, and V. Vasilyev, Preparation of rare metallic actinides (248Cm,249Bk,249Cf) and investigation of their crystal structure, *Journal of Radioanalytical and Nuclear Chemistry* **143**, 253 (1990).
- [112] R. Wyckoff, Fluorite structure, *Crystal structures* **1**, 239 (1963).
- [113] A. P. Koufos and D. A. Papaconstantopoulos, Electronic structure of francium, *International Journal of Quantum Chemistry* **113**, 2070 (2013).
- [114] W. H. Beamer and C. R. Maxwell, Physical Properties of Polonium. II. X-Ray Studies and Crystal Structure, *The Journal of Chemical Physics* **17**, 1293 (1949).
- [115] M. A. Rollier, S. B. Hendricks, and L. R. Maxwell, The Crystal Structure of Polonium by Electron Diffraction, *The Journal of Chemical Physics* **4**, 648 (1936).
- [116] K. Bagnall and R. d'Eye, The preparation of polonium metal and polonium dioxide, *Journal of the Chemical Society (Resumed)* , 4295 (1954).
- [117] A. Menad, A. Zaoui, and M. Ferhat, Two novel stable phases of polonium oxides from first-principles evolutionary algorithm, *Computational Condensed Matter* **40**, e00933 (2024).
- [118] A. I. Khojandi and D. A. Papaconstantopoulos, Electronic structure calculations and determination of related properties for radium, *Phys. Rev. B* **82**, 155121 (2010).
- [119] O. R. Smits, P. Jerabek, E. Pahl, and P. Schwerdtfeger, A Hundred-Year-Old Experiment Re-evaluated: Accurate Ab Initio Monte Carlo Simulations of the Melting of Radon, *Angewandte Chemie International Edition* **57**, 9961 (2018).
- [120] G. E. R. Schulze, Die Kristallstruktur von Radiumfluorid, *Zeitschrift für Physikalische Chemie* **32B**, 430 (1936).
- [121] A. V. Matyskin, R. Ylmen, P. Lagerkvist, H. Ramebäck, and C. Ekberg, Crystal structure of radium sulfate: An X-ray powder diffraction and density functional theory study, *Journal of Solid State Chemistry* **253**, 15 (2017).
- [122] C. Pimentel, C. M. Pina, and C. I. Sainz-Díaz, New Insights into Dolomite and Dolomite-Analogue Structures from First Principles Calculations, *ACS Earth and Space Chemistry* **6**, 2360 (2022).
- [123] W. Witteman, A. Giorgi, and D. Vier, The Preparation and Identification of Some Intermetallic Compounds of POLONIUM<sup>1</sup>, *The Journal of Physical Chemistry* **64**, 434 (1960).
- [124] E. Prokin, B. Aksenov, N. Chebotarev, and Z. Ershova, Titanium, zirconium and hafnium monopolonides, *Radiokhimiya* **20**, 684–686 (1978).
- [125] K. Bagnall, R. D'Eye, and J. Freeman, The polonium halides. Part I. Polonium chlorides, *Journal of the Chemical Society (Resumed)* , 2320 (1955).
- [126] K. Bagnall, R. d'Eye, and J. Freeman, The polonium halides. Part II. bromides, *Journal of the Chemical Society (Resumed)* , 3959 (1955).
- [127] C. Kershner, R. DeSando, R. Heidelberg, and R. Steinmeyer, Rare earth polonides, *Journal of Inorganic and Nuclear Chemistry* **28**, 1581 (1966).
- [128] J. P. Charvillat, U. Benedict, D. Damien, and W. Muller, Preparation and lattice parameters of some americium and curium pnictides, *Radiochem. Radioanal. Lett.*, v. 20, no. 6, pp. 371-381 (1975).
- [129] M. Gensini, R. Haire, U. Benedict, and F. Hulliger, High-pressure behavior of CmBi and UBi, *Physica B: Condensed Matter* **190**, 75 (1993).
- [130] R. E. Sykora, Z. Assefa, R. G. Haire, and T. E. Albrecht-Schmitt, Hydrothermal synthesis, structure, Raman spectroscopy, and self-irradiation studies of 248Cm(IO<sub>3</sub>)<sub>3</sub>, *Journal of Solid State Chemistry* **177**, 4413 (2004).
- [131] M. J. Polinski, D. J. Grant, S. Wang, E. V. Alekseev, J. N. Cross, E. M. Villa, W. Depmeier, L. Gagliardi, and T. E. Albrecht-Schmitt, Differentiating between Trivalent Lanthanides and Actinides, *Journal of the American Chemical Society* **134**, 10682 (2012).
- [132] S. K. Cary, M. A. Silver, G. Liu, J. C. Wang, J. A. Bogart, J. T. Stritzinger, A. A. Arico, K. Hanson, E. J. Schelter, and T. E. Albrecht-Schmitt, Spontaneous Partitioning of Californium from Curium: Curious Cases from the Crystallization of Curium Coordination Complexes, *Inorganic Chemistry* **54**, 11399 (2015).
- [133] R. Oldenbourg, The Cu<sub>2</sub>Sb and related structures, *Zeitschrift Für Kristallographie* **170**, 23 (1985).
- [134] M. J. Polinski, E. B. Garner III, R. Maurice, N. Planas, J. T. Stritzinger, T. G. Parker, J. N. Cross, T. D. Green, E. V. Alekseev, S. M. Van Cleve, *et al.*, Unusual structure, bonding and properties in a californium borate, *Nature chemistry* **6**, 387 (2014).
- [135] R. Baybarz, J. Fahey, and R. Haire, The preparation, crystal structures and some properties of californium oxysulfate and oxysulfide, *Journal of Inorganic and Nuclear Chemistry* **36**, 2023 (1974).
- [136] J. Peterson and J. H. Burns, Preparation and crystal structure of californium oxyfluoride, CfOF, *Journal of Inorganic and Nuclear Chemistry* **30**, 2955 (1968).
- [137] R. E. Sykora, Z. Assefa, R. G. Haire, and T. E. Albrecht-Schmitt, First Structural Determination of a Trivalent Californium Compound with Oxygen Coordination, *Inorganic Chemistry* **45**, 475 (2006).
- [138] F. Ellinger and W. H. Zachariasen, The Crystal Structure of KPUO<sub>2</sub>CO<sub>3</sub>, NH<sub>4</sub>PUO<sub>2</sub>CO<sub>3</sub> and RbAMO<sub>2</sub>CO<sub>3</sub>, *The Journal of Physical Chemistry* **58**, 405 (1954).
- [139] F. Weigel, V. Wishnevsky, and M. Wolf, The crystal structure of americium(III) oxybromide, *Journal of the Less Common Metals* **63**, 81 (1979).
- [140] A. Tabuteau and M. Pagès, Etude cristallographique du molybdate et du tungstate d'américium(III): alpha-Am<sub>2</sub>(MoO<sub>4</sub>)<sub>3</sub>, alpha-Am<sub>2</sub>(WO<sub>4</sub>)<sub>3</sub>, *Journal of Solid State Chemistry* **26**, 153 (1978).
- [141] J. N. Cross, T.-H. Lee, C.-J. Kang, Y.-X. Yao, S. K. Cary, J. T. Stritzinger, M. J. Polinski, C. D. McKinley, T. E. Albrecht Schmitt, and N. Lanata, Origins of the odd optical observables in plutonium and americium tungstates, *Chem. Sci.* **10**, 6508 (2019).
- [142] J. Su, T. Cheisson, A. McSkimming, C. A. P. Goodwin, I. DiMucci, T. Albrecht-Schönzart, B. L. Scott, E. R. Batista, A. J. Gaunt, S. A. Kozimor, P. Yang, and E. J. Schelter, Complexation and redox chemistry of neptunium, plutonium and americium with a hydroxylaminate ligand, *Chem. Sci.* **12**, 13343 (2021).
- [143] M. S. Grigoriev and A. M. Fedosseev, Sodium tris(acetato- $\kappa^2 O, O'$ )dioxidoamericatate(VI) and guanidinium tris(cyclopropanecarboxylato- $\kappa^2 O, O'$ )dioxidoamericatate(VI), *Acta Crystallographica Section C* **67**, m205 (2011).

- [144] R. Baybarz, L. Asprey, C. Strouse, and E. Fukushima, Divalent americium: The crystal structure and magnetic susceptibility of AmI<sub>2</sub>, *Journal of Inorganic and Nuclear Chemistry* **34**, 3427 (1972).
- [145] L. B. Asprey, F. H. Ellinger, and W. H. Zachariasen, Preparation, Identification and Crystal Structure of a Pentavalent Americium Compound, KAmO<sub>2</sub>F<sub>21</sub>, *Journal of the American Chemical Society* **76**, 5235 (1954).
- [146] S. S. Galley, A. A. Arico, T.-H. Lee, X. Deng, Y.-X. Yao, J. M. Sperling, V. Proust, J. S. Storbeck, V. Dobrosavljevic, J. N. Neu, T. Siegrist, R. E. Baumbach, T. E. Albrecht-Schmitt, N. Kaltsoyannis, and N. Lanatà, Uncovering the Origin of Divergence in the CsM(CrO<sub>4</sub>)<sub>2</sub> (M = La, Pr, Nd, Sm, Eu; Am) Family through Examination of the Chemical Bonding in a Molecular Cluster and by Band Structure Analysis, *Journal of the American Chemical Society* **140**, 1674 (2018).
- [147] W. Runde, A. C. Bean, L. F. Brodnax, and B. L. Scott, Synthesis and Characterization of f-Element Iodate Architectures with Variable Dimensionality, alpha- and beta-Am(IO<sub>3</sub>)<sub>3</sub>, *Inorganic Chemistry* **45**, 2479 (2006).
- [148] R. E. Sykora, Z. Assefa, R. G. Haire, and T. E. Albrecht-Schmitt, Synthesis, Structure, and Spectroscopic Properties of Am(io<sub>3</sub>)<sub>3</sub> and the Photoluminescence Behavior of Cm(IO<sub>3</sub>)<sub>3</sub>, *Inorganic Chemistry* **44**, 5667 (2005).
- [149] J. N. Cross, E. M. Villa, S. Wang, J. Diwu, M. J. Polinski, and T. E. Albrecht-Schmitt, Syntheses, structures, and spectroscopic properties of plutonium and americium phosphites and the redetermination of the ionic radii of Pu (III) and Am (III), *Inorganic Chemistry* **51**, 8419 (2012).
- [150] J. H. Burns and R. D. Baybarz, Crystal structure of americium sulfate octahydrate, *Inorganic Chemistry* **11**, 2233 (1972).
- [151] C. Tamain, B. Arab-Chapelet, M. Rivenet, X. F. Legoff, G. Loubert, S. Grandjean, and F. Abraham, Coordination Modes of Americium in the Am<sub>2</sub>(C<sub>2</sub>O<sub>4</sub>)<sub>3</sub>(H<sub>2</sub>O)<sub>6</sub>·4H<sub>2</sub>O Oxalate: Synthesis, Crystal Structure, Spectroscopic Characterizations and Comparison in the M<sub>2</sub>(C<sub>2</sub>O<sub>4</sub>)<sub>3</sub>(H<sub>2</sub>O)<sub>6</sub>·nH<sub>2</sub>O (M = Ln, An) Series, *Inorganic Chemistry* **55**, 51 (2016).
- [152] S. K. Cary, J. Su, S. S. Galley, T. E. Albrecht-Schmitt, E. R. Batista, M. G. Ferrier, S. A. Kozimor, V. Mocko, B. L. Scott, C. E. Van Alstine, F. D. White, and P. Yang, A series of dithiocarbamates for americium, curium, and californium, *Dalton Trans.* **47**, 14452 (2018).
- [153] W. Runde, A. C. Bean, and B. L. Scott, Synthesis and characterization of a channel framework in K<sub>3</sub>Am<sub>3</sub>(IO<sub>3</sub>)<sub>12</sub>·HIO<sub>3</sub>, *Chem. Commun.* , 1848 (2003).
- [154] R. E. Wilson, T. J. Carter, M. Autillo, and S. Stegman, Thiocyanate complexes of the lanthanides, Am and Cm, *Chem. Commun.* **56**, 2622 (2020).
- [155] Z. K. Huffman, J. M. Sperling, C. J. Windorff, B. N. Long, L. Cordova, H. Ramanantoanina, C. Celis-Barros, and T. E. Albrecht-Schönzart, Synthesis and characterization of a bimetallic americium(III) pyrrithionate coordination complex, *Chem. Commun.* **58**, 11791 (2022).
- [156] C. Xu, T. Liu, Q. Liu, S. Yang, D. Li, and G. Tian, Complexation of Am(III) and Eu(III) with DRAPA (N,N-dialkyl-6-amide-pyridine-2-carboxylic acid), *Dalton Trans.* **52**, 15669 (2023).
- [157] P. Villars, K. Cenzual, and R. Gladyshevskii, *Handbook* (De Gruyter, Berlin, Boston, 2017).
- [158] A. Zalkin and D. H. Templeton, The crystal structures of CeB<sub>4</sub> ThB<sub>4</sub> and UB<sub>4</sub>, *Acta Crystallographica* **6**, 269 (1953).
- [159] R. Wang and H. Steinfink, The crystal chemistry of selected AB<sub>2</sub> rare earth compounds with selenium, tellurium, and antimony, *Inorganic Chemistry* **6**, 1685 (1967).
- [160] N. J. Nisha, M. B. Mansur, M. B. H. Parosh, R. N. Mondal, and M. R. Islam, Apply to the Field of Optoelectronics by Examining Structural, Electronic, Optical, Mechanical, and Thermophysical Properties of FrBeX<sub>3</sub> (X = Cl and Br) Perovskites, *Nano Select* **7**, e70095 (2026).
- [161] M. B. Mansur, F. Farhan, N. J. Nisha, M. B. H. Parosh, B. N. Anam, I. A. Ovi, J. Y. Al-Humaidi, and M. R. Islam, Pressure-influenced comparative investigation of electronic, structural, and mechanical properties of non-toxic halide perovskites FrCaX<sub>3</sub> (X= Cl, Br, and I): A first-principles investigation for advanced optoelectronic applications, *Journal of Inorganic and Organometallic Polymers and Materials* **35**, 7487 (2025).
- [162] M. I. Ahmed, A. Biswas, T. I. Asif, M. Saiduzzaman, and M. Islam, Hydrostatic pressure-induced transformations and multifunctional properties of Francium-based halide perovskite FrCaCl<sub>3</sub>: Insights from first-principles calculations, *Heliyon* **10**, e34059 (2024).
- [163] M. S. Nawaz Romel, F. T. Zohra, A. Al Rashid, and I. A. Ovi, First-principle calculation of the physical properties of tri-halide perovskite FrSrX<sub>3</sub> (X = F, Cl, Br, and I): A DFT study, *AIP Advances* **15**, 105032 (2025).
- [164] N. J. Nisha, M. Saiduzzaman, M. B. H. Parosh, I. A. Ovi, and D. Choi, Novel Lead-Free Perovskites FrZnX<sub>3</sub> (X = F, Cl, and Br) for Optoelectronics Applications: A DFT Study, *International Journal of Energy Research* **2025**, 5549809 (2025).
- [165] M. D. R. Hasan, I. A. Apon, I. A. Ovi, and M. S. Haque, Calculations of the mechanical, optoelectronic, and magnetic properties of FrGeX<sub>3</sub> (X = Cl, Br, I) under hydrostatic pressures based on first-principles theories, *AIP Advances* **14**, 035341 (2024).
- [166] I. A. Apon, M. D. Ratul Hasan, I. A. Ovi, and Fatema-Tuz-Zahra, Pressure-driven semiconducting to metallic transition in francium tin trihalides perovskite with improved optoelectronic performance: A DFT study, *AIP Advances* **14**, 065126 (2024).
- [167] P. Butkalyuk, I. Butkalyuk, S. Tomilin, A. Kupriyanov, R. Abdullof, A. Kolobova, and K. Rotmanov, A study of the Interaction of Radium Salts with Construction Materials, *Radiochemistry* **63**, 307 (2021).
- [168] P. Butkalyuk, I. Butkalyuk, R. Kuznetsov, and S. Tomilin, Synthesis and X-ray diffraction study of radium plumbate, *Radiochemistry* **55**, 41 (2013).
- [169] P. B. Romero-Vázquez and S. López-Moreno, Ab initio study of RaWO<sub>4</sub>: Comparison with isoelectronic tungstates, *Journal of Solid State Chemistry* **317**, 123709 (2023).
- [170] M.-S. Liao and Q.-E. Zhang, Chemical Bonding in XeF<sub>2</sub>, XeF<sub>4</sub>, KrF<sub>2</sub>, KrF<sub>4</sub>, RnF<sub>2</sub>, XeCl<sub>2</sub>, and XeBr<sub>2</sub>: From the Gas Phase to the Solid State, *The Journal of Physical Chemistry A* **102**, 10647 (1998).

TABLE III. Literature and database sources for initial Basic Heavy Element (BHE) subset structures.

COD ID	Primitive Formula	Structure type	Crystal System	Space Group No.	Ref.
9008524	Am	dhcp	hexagonal	194	[101]
-	Am	fddd	orthorhombic	70	[102]
-	Am	hcp	hexagonal	194	This work
-	Am	Pnma	orthorhombic	62	[102]
-	Am <sub>2</sub> O <sub>3</sub>	A-type	trigonal	164	[103]
4124688	Am <sub>2</sub> O <sub>3</sub>	C-type	cubic	206	[104]
9008998	AmO <sub>2</sub>	fluorite	cubic	225	[101]
-	At	bcc	cubic	229	[105]
-	At	bct	tetragonal	139	[105]
-	At	fcc	cubic	225	[105]
-	At	hcp	hexagonal	194	[105]
-	Cf	bcc	hexagonal	229	This work
-	Cf	dhcp	hexagonal	194	[106]
-	Cf	fcc	cubic	225	[106]
-	Cf	fddd	orthorhombic	70	[106]
-	Cf	hcp	hexagonal	194	This work
-	CfO	NaCl	cubic	225	[107]
-	CfO <sub>2</sub>	fluorite	cubic	225	[108]
-	Cm	bcc	cubic	229	This work
-	Cm	dhcp	hexagonal	194	[109]
-	Cm	fcc	cubic	225	[109]
-	Cm <sub>2</sub> O <sub>3</sub>	A-type	trigonal	164	[110]
1528054	CmO	NaCl	cubic	225	[111]
9009009	CmO <sub>2</sub>	fluorite	cubic	225	[112]
-	Fr	bcc	cubic	229	[113]
-	Fr	fcc	cubic	225	[113]
-	Fr	hcp	hexagonal	194	[113]
1509138	Po	alpha	cubic	221	[114]
-	Po	bcc	cubic	229	This work
1537759	Po	beta	trigonal	166	[114]
-	Po	fcc	cubic	225	This work
-	Po	hcp	hexagonal	194	This work
1010519	Po	monoclinic	monoclinic	5	[115]
1534201	PoO <sub>2</sub>	fluorite	cubic	225	[116]
-	PoO <sub>2</sub>	Pmn21	orthorhombic	31	[117]
-	Ra	bcc	cubic	229	[118]
-	Ra	fcc	cubic	225	[118]
-	Ra	hcp	hexagonal	194	[118]
-	RaO	NaCl	cubic	225	This work
-	Rn	bcc	cubic	229	This work
-	Rn	fcc	cubic	225	[119]
-	Rn	hcp	Hexagonal	194	[119]

TABLE IV. Literature and database sources for initial Complex Heavy Element (CHE) subset structures.

COD ID	Primitive Formula	Structure type	Crystal System	Space Group No.	Ref.
1010655	RaF <sub>2</sub>	fluorite	cubic	225	[120]
3000125	BaRa <sub>3</sub> S <sub>4</sub> O <sub>16</sub>	barite	orthorhombic	62	[121]
4519447	MgRaC <sub>2</sub> O <sub>6</sub>	-	trigonal	166	[122]
1523087	PbPo	NaCl	cubic	225	[123]
1523090	HgPo	NaCl	cubic	225	[123]
1525466	CdPo	ZnS	cubic	216	[123]
1530616	HfPo	NiAs	hexagonal	194	[124]
1534202	PoCl <sub>2</sub>	-	orthorhombic	47	[125]
1541440	Cs <sub>2</sub> PoBr <sub>6</sub>	K <sub>2</sub> PtCl <sub>6</sub>	cubic	225	[126]
4031181	LuPo	NaCl	cubic	225	[127]
4031186	HoPo	NaCl	cubic	225	[127]
4031200	DyPo	NaCl	cubic	225	[127]
4031201	EuPo	NaCl	cubic	225	[127]
1008976	CmAs	NaCl	cubic	225	[128]
1527406	CmBi	NaCl	cubic	225	[129]
1535304	CmI <sub>3</sub> O <sub>9</sub>	-	monoclinic	14	[130]
4118157	Cm <sub>2</sub> B <sub>14</sub> ClO <sub>29</sub>	-	monoclinic	14	[131]
4346740	C <sub>28</sub> H <sub>35</sub> Cl <sub>4</sub> Cm <sub>2</sub> N <sub>4</sub> O <sub>25</sub>	-	triclinic	2	[132]
9008339	CmS <sub>2</sub>	UAs <sub>2</sub>	tetragonal	129	[133]
9008340	CmSe <sub>2</sub>	UAs <sub>2</sub>	tetragonal	129	[133]
1552049	CfB <sub>6</sub> H <sub>5</sub> O <sub>13</sub>	-	monoclinic	15	[134]
4031557	Cf <sub>2</sub> O <sub>2</sub> S	-	trigonal	164	[135]
4031662	CfOF	fluorite	cubic	225	[136]
4300618	CfI <sub>3</sub> O <sub>9</sub>	-	monoclinic	14	[137]
1527345	RbAmCO <sub>5</sub>	-	hexagonal	194	[138]
1530991	AmOBr	PbFCl	tetragonal	129	[139]
1539269	Am <sub>2</sub> Mo <sub>2</sub> O <sub>8</sub>	-	tetragonal	88	[140]
1551090	AmHWO <sub>5</sub>	-	monoclinic	14	[141]
1564665	C <sub>54</sub> H <sub>78</sub> Am <sub>2</sub> N <sub>12</sub> O <sub>6</sub>	-	monoclinic	14	[142]
2018120	C <sub>6</sub> H <sub>9</sub> AmNaO <sub>8</sub>	-	cubic	198	[143]
2018121	C <sub>13</sub> H <sub>21</sub> AmN <sub>3</sub> O <sub>8</sub>	-	monoclinic	14	[143]
4031505	AmI <sub>2</sub>	-	monoclinic	14	[144]
4031506	AmOI	PbFCl	tetragonal	129	[144]
4118156	AmB <sub>9</sub> O <sub>18</sub>	-	monoclinic	14	[131]
4124620	KAmO <sub>2</sub> F <sub>2</sub>	-	trigonal	166	[145]
4124687	AmOCl	PbFCl	tetragonal	129	[104]
4127110	CsAmCr <sub>2</sub> O <sub>8</sub>	-	triclinic	2	[146]
4127111	CsAmCr <sub>2</sub> O <sub>8</sub>	-	monoclinic	13	[146]
4300606	AmI <sub>3</sub> O <sub>9</sub>	-	monoclinic	14	[147]
4309330	AmI <sub>3</sub> O <sub>9</sub>	-	monoclinic	14	[148]
4329911	Am <sub>2</sub> P <sub>3</sub> O <sub>10</sub>	-	monoclinic	15	[149]
4343599	Am <sub>2</sub> H <sub>16</sub> S <sub>3</sub> O <sub>20</sub>	-	monoclinic	15	[150]
4346616	C <sub>6</sub> H <sub>12</sub> Am <sub>2</sub> O <sub>23</sub>	-	monoclinic	14	[151]
7047397	C <sub>27</sub> H <sub>38</sub> AmN <sub>5</sub> S <sub>6</sub>	-	monoclinic	14	[152]
7103819	K <sub>3</sub> Am <sub>3</sub> HI <sub>13</sub> O <sub>39</sub>	-	trigonal	161	[153]
7125922	C <sub>39</sub> AmN <sub>11</sub> S <sub>7</sub>	-	cubic	221	[154]
7130789	C <sub>15</sub> H <sub>20</sub> AmN <sub>3</sub> O <sub>7</sub> S <sub>3</sub>	-	triclinic	2	[155]
7713802	C <sub>27</sub> H <sub>27</sub> AmN <sub>6</sub> O <sub>9</sub>	-	Monoclinic	14	[156]

TABLE V: Literature and additional database sources beyond COD for initial Complex Heavy Element (CHE) subset structures.

COD ID	Primitive Formula	Structure type	Crystal System	Space Group No.	Ref.
-	AmPd <sub>3</sub>	Cu <sub>3</sub> Au	cubic	221	[157]
-	Am <sub>12</sub> S <sub>16</sub>	Th <sub>3</sub> P <sub>4</sub>	cubic	220	[157]
-	Am <sub>12</sub> Se <sub>16</sub>	Th <sub>3</sub> P <sub>4</sub>	cubic	220	[157]
-	Am <sub>12</sub> Te <sub>16</sub>	Th <sub>3</sub> P <sub>4</sub>	cubic	220	[157]
-	Am <sub>12</sub> Sb <sub>16</sub>	Th <sub>3</sub> P <sub>4</sub>	cubic	220	[157]
-	Am <sub>4</sub> As <sub>4</sub>	NaCl	cubic	225	[157]
-	Am <sub>4</sub> Bi <sub>4</sub>	NaCl	cubic	225	[157]
-	Am <sub>8</sub> Fe <sub>16</sub>	MgCu <sub>2</sub>	cubic	227	[157]
-	Am <sub>4</sub> H <sub>8</sub>	CaF <sub>2</sub>	cubic	225	[157]
-	Am <sub>8</sub> Ir <sub>16</sub>	MgCu <sub>2</sub>	cubic	227	[157]
-	AmLa <sub>3</sub>	Cu <sub>3</sub> Au	cubic	221	[157]
-	Am <sub>12</sub> N <sub>16</sub>	Th <sub>3</sub> P <sub>4</sub>	cubic	220	[157]
-	Am <sub>4</sub> N <sub>4</sub>	NaCl	cubic	225	[157]
-	Am <sub>8</sub> Ni <sub>16</sub>	MgCu <sub>2</sub>	cubic	227	[157]
-	Am <sub>4</sub> O <sub>4</sub>	NaCl	cubic	225	[157]
-	Am <sub>8</sub> Rh <sub>16</sub>	MgCu <sub>2</sub>	cubic	227	[157]
-	AmRh <sub>3</sub>	Cu <sub>3</sub> Au	cubic	221	[157]
-	Am <sub>4</sub> S <sub>4</sub>	NaCl	cubic	225	[157]
-	AmSi <sub>2</sub>	AlB <sub>2</sub>	hexagonal	191	[157]
-	AmTe	CsCl	cubic	221	[157]
-	Am <sub>4</sub> Te <sub>4</sub>	NaCl	cubic	225	[157]
-	AmCu <sub>5</sub>	CaCu <sub>5</sub>	hexagonal	191	[157]
-	AmB <sub>4</sub>	UB <sub>4</sub>	tetragonal	127	[158]
-	AmB <sub>6</sub>	CaB <sub>6</sub>	cubic	221	[157]
-	AmCl	CsCl	cubic	221	[157]
-	AmSb <sub>2</sub>	SmSb <sub>2</sub>	orthorhombic	64	[159]
-	Cf <sub>4</sub> S <sub>4</sub>	NaCl	cubic	225	[157]
-	Cf <sub>4</sub> Sb <sub>4</sub>	NaCl	cubic	225	[157]
-	CmCo <sub>2</sub>	MgCu <sub>2</sub>	cubic	227	[157]
-	CmCo <sub>5</sub>	CaCu <sub>5</sub>	hexagonal	191	[157]
-	CmFe <sub>2</sub>	MgCu <sub>2</sub>	cubic	227	[157]
-	CmH <sub>2</sub>	CaF <sub>2</sub>	cubic	225	[157]
-	CmIr <sub>3</sub>	Cu <sub>3</sub> Au	cubic	221	[157]
-	CmN	NaCl	cubic	225	[157]
-	CmNi <sub>3</sub>	Cu <sub>3</sub> Au	cubic	221	[157]
-	CmNi <sub>5</sub>	CaCu <sub>5</sub>	hexagonal	191	[157]
-	CmP	NaCl	cubic	225	[157]
-	CmPt <sub>3</sub>	Cu <sub>3</sub> Au	cubic	221	[157]
-	CmPt <sub>5</sub>	CaCu <sub>5</sub>	hexagonal	191	[157]
-	CmRh <sub>2</sub>	MgCu <sub>2</sub>	cubic	227	[157]
-	CmRh <sub>3</sub>	Cu <sub>3</sub> Au	cubic	221	[157]
-	CmS	NaCl	cubic	225	[157]
-	CmSb	NaCl	cubic	225	[157]
-	CmSe	NaCl	cubic	225	[157]
-	CmTe	NaCl	cubic	225	[157]
-	CmH <sub>3</sub>	Na <sub>3</sub> As	hexagonal	194	[157]
-	CmRu <sub>2</sub>	MgZn <sub>2</sub>	hexagonal	194	[157]
-	FrBeBr <sub>3</sub>	perovskite	cubic	221	[160]
-	FrBeCl <sub>3</sub>	perovskite	cubic	221	[160]
-	FrCaBr <sub>3</sub>	perovskite	cubic	221	[161]
-	FrCaCl <sub>3</sub>	perovskite	cubic	221	[161, 162]
-	FrCaI <sub>3</sub>	perovskite	cubic	221	[161]
-	FrSrBr <sub>3</sub>	perovskite	cubic	221	[163]
-	FrSrCl <sub>3</sub>	perovskite	cubic	221	[163]
-	FrSrF <sub>3</sub>	perovskite	cubic	221	[163]
-	FrSrI <sub>3</sub>	perovskite	cubic	221	[163]
-	FrZnBr <sub>3</sub>	perovskite	cubic	221	[164]
-	FrZnCl <sub>3</sub>	perovskite	cubic	221	[164]
-	FrZnF <sub>3</sub>	perovskite	cubic	221	[164]

*Continued on next page*

COD ID	Primitive Formula	Structure type	Crystal System	Space Group No.	Ref.
-	FrGeBr <sub>3</sub>	perovskite	cubic	221	[165]
-	FrGeCl <sub>3</sub>	perovskite	cubic	221	[165]
-	FrGeI <sub>3</sub>	perovskite	cubic	221	[165]
-	FrSnBr <sub>3</sub>	perovskite	cubic	221	[166]
-	FrSnCl <sub>3</sub>	perovskite	cubic	221	[166]
-	FrSnI <sub>3</sub>	perovskite	cubic	221	[166]
-	RaS	NaCl	cubic	225	[157]
-	RaSe	NaCl	cubic	225	[157]
-	RaCrO <sub>4</sub>	barite	orthorhombic	62	[167]
-	RaPbO <sub>3</sub>	perovskite	cubic	221	[168]
-	RaSO <sub>4</sub>	barite	orthorhombic	62	[121]
-	RaWO <sub>4</sub>	scheelite	tetragonal	88	[169]
-	RnF <sub>2</sub>	XeF <sub>2</sub>	tetragonal	139	[170]